1 2 9 0

UNIVERSIDADE D
COIMBRA

Pedro Mota Gil Agostinho

DESENVOLVIMENTO DE IMPLANTES DENTÁRIOS

VOLUME 1

Dissertação no âmbito do Mestrado Integrado em Engenharia Mecânica na especialidade de Energia e Ambiente orientada pela Professora Doutora Sandra Maria Fernandes Carvalho e apresentada à unidade orgânica de Dissertação de Mestrado, ao Departamento de Engenharia Mecânica.

.

Outubro de 2021

FACULDADE DE CIÊNCIAS E TECNOLOGIA
UNIVERSIDADE D COIMBRA

Development of Dental Implants

Submitted in Partial Fulfilment of the Requirements for the Degree of Master in Mechanical Engineering in the speciality of Energy and Environment

Desenvolvimento de Implantes Dentários

Author

Pedro Mota Gil Agostinho

Advisors

Sandra Carvalho

Jury

President	**Professor Doutor Albano Augusto Cavaleiro Rodrigues de Carvalho**
Vowel[s]	**Professor Doutor Cristiana Filipa Almeida Alves**
	Professor Doutor Sandra Maria Fernandes Carvalho
Advisor	**Professor Doutor Sandra Maria Fernandes Carvalho**

Coimbra, October, 2021

ACKNOWLEDGEMENTS

This Thesis represents the ending of an important stage of my life. Throughout my path I was positively influenced by a number of friends, family and mentors to whom I would like to thank.

To my advisor Professor Sandra Carvalho, for the guidance and disponibility.

To Professor Albano Cavaleiro and Engineer Nuno Figueiredo, for all the help, knowledge and advice.

To the collaborators of IPN, for providing me the space and conditions to do the experiments and for helping me settle in.

To the group from Minho's University, to Cristiana, Luísa, Catarina, Sandra Mariana, Edgar and Edith for all the help and patience to transmit to me the knowledge I needed during this journey.

To ZGs, my group of friends, for all the adventures, smiles and support.

To my grandparents, for being great role models who inspire me every day.

To my parents and my sister, for the help, strength and motivation which they guide me with every day.

And finally, to Margarida, my girlfriend, for all the love, patience and motivation to always be a better version of myself.

To everyone, Thank You.

Abstract

Dental implants are susceptible to bacterial infections such as Peri-implantitis. This pathological condition is initiated by a bacterial biofilm that adheres and surrounds the dental implant, which triggers the inflammation of soft tissues and loss of supporting bone. Furthermore, if not addressed in time this disease may lead to osseointegration failure and consequent implant failure. Therefore, with the objective of minimizing the impact of bacteria adhesion on the implant, this thesis proposes the deposition of bactericidal silver nanoparticles on a tantalum (Ta) nanostructured surface.

In this thesis, tantalum oxide nanostructures were obtained by submitting regular tantalum sheets to Plasma Electrolytic Oxidation, which created micro and nanopores on the Ta surface. Afterwards, silver nanoparticles were sputtered onto the nanostructured substrate in order to obtain nanoparticles with different sizes. Then, some of these deposited substrates were covered with a thin layer of carbon to analyze its impact on the silver ion release (well known as the active antimicrobial agent) as well as the structural robustness of the samples.

Silver ion release revealed that the amount of silver nanoparticles deposited were not enough to generate an antibacterial activity capable of preventing an infection. However, these results also proved that the nano-galvanic couple of silver and carbon enhances the ionization of the biocidal Ag^{+}. This thesis also shows that the carbon layer possesses the promising ability of improving the mechanical robustness of the samples.

Keywords Silver Nanoparticles, Tantalum, Antibacterial Activity, Nanostructures, Carbon.

Resumo

Implantes dentários são dispositivos suscetíveis a infeções bacterianas como a peri-implantite. Esta condição patológica começa pela criação de um biofilme bacteriano que adere e rodeia o implante dentário, resultando na inflamação dos tecidos moles e perda de osso. Além disso, se esta doença for negligenciada, podem ocorrer falhas na osteointegração e consequente perda do implante. Portanto, com o objetivo de minimizar o impacto da colonização bacteriana no implante, esta tese propõe a deposição de nanopartículas bactericidas de prata numa superfície nanoestruturada de Tântalo (Ta).

Nesta tese, as nanoestruturas de óxido de Tântalo foram obtidas através da Oxidação por Plasma Eletrolítico de chapas de Ta, o que permitiu obter micro e nanoporos na sua superfície. Nanopartículas de prata (Ag NPs) foram pulverizadas nos substratos nanoestruturados com o objetivo de obter nanopartículas com diferentes tamanhos. Posteriormente, alguns dos substratos depositados com NPs de prata foram cobertos com uma fina camada de carbono para estudar como seria o seu impacto na libertação de iões de prata e na resistência mecânica da amostra.

Os níveis de libertação iónica de prata revelaram que a quantidade de nanopartículas de prata depositadas não foram suficientes para produzir uma atividade antibacteriana capaz de prevenir infeções. Contudo, estes resultados provaram que o par nano-galvânico entre a prata e o carbono aumentou a quantidade de Ag^+ biocida que é ionizada, além de que a camada de carbono permitiu encapsular efetivamente as NPs conferindo-lhes uma maior resistência mecânica e adesão à superfície de tântalo nanoestruturado.

Palavras-chave: Nanopartículas de prata, Tântalo, Atividade antibacteriana, Nanoestruturas, Carbono.

Contents

LIST OF FIGURES

LIST OF TABLES

LIST OF SIMBOLS AND ACRONYMS/ ABBREVIATIONS

List of Symbols

$\boldsymbol{Ag}$ – Silver

$\boldsymbol{C}$ – Carbon

$\boldsymbol{Cu}$ – Copper

$\boldsymbol{Zn}$ – Zinc

$\boldsymbol{P}$ – Phosphate

$\boldsymbol{Ti}$ – Titanium

$\boldsymbol{O}$ – Oxygen

$\boldsymbol{Mn}$ – Manganese

$\boldsymbol{Fe}$ – Iron

$\boldsymbol{Nb}$ – Niobium

$\boldsymbol{Ta}$ – Tantalum

m – Mass

M – Molar Mass

L – Litre

Sa – Area Mean Roughness

Sq – Area Square Roughness

Acronyms/Abbreviations

NPs – Nanoparticles

ROS – Reactive Oxygen Species

UV – Ultraviolet

WHO – World Health Organization

DNA – Deoxyribonucleic Acid

Ag NPs – Silver Nanoparticles

MAO – Microarc Oxidation

PVD – Physical Vapor Deposition

PEO – Plasma Electrolytic Oxidation

DC – Direct Current

Ta_CaP – Tantalum oxide substrate dopped with calcium and phosphate

Ta_CaP_1nmAg– Tantalum oxide substrate dopped with calcium and phosphate, deposited with 1nm silver nanoparticles

Ta_CaP_2nmAg– Tantalum oxide substrate dopped with calcium and phosphate, deposited with 2nm silver nanoparticles

Ta_CaP_1nmAg_C– Tantalum oxide substrate dopped with calcium and phosphate, deposited with 1nm silver nanoparticles and carbon

Ta_CaP_2nmAg– Tantalum oxide substrate dopped with calcium and phosphate, deposited with 2nm silver nanoparticles and carbon

XRD – X-Ray Diffraction Microscopy

AFM – X Atomic Force Microscopy

SEM – Scanning Electron Microscopy

EDS – Energy Dispersive X-ray Spectroscopy

ICP-OES – Inductively Coupled Plasma Optical Emission Spectroscopy

ICDD – International Center for Diffraction Data

1. INTRODUCTION

Teeth are very important bone structures that interfere in a person's mastication, speech, and social integration. Therefore, teeth loss can be a devastating occurrence that may require surgical dental implants.

Dental implants are devices used to replace lost teeth. In order to apply dental implants, patients must be submitted to surgery. Even though these surgeries present high success rates there are still long-term problems that arise such as slow osseointegration and peri-implantitis infection. The previously mentioned complications are a problematic outcome of the adhesion of bacteria to the device which form a biofilm and lead to the recession of bone tissue. The bacterial infections that derive from surgery might require antibiotics and, in extreme cases, when the implant is unable to fuse with the bone, the patient must be submitted to new surgery and remove the implant as well as the infected bone tissue.

Titanium (Ti) is the most used material in dental implant applications. This metal is mostly used because it has biocompatibility and therefore good interactivity with adjacent tissues. However, titanium-based implants present two major shortcomings. Firstly, although Ti has some bioactivity it can be insufficient in some cases and lead to slow osseointegration and consequent bacterial inflammation. The second problem is the lack of antibacterial properties of these implants which can require patients to take antibiotics in order to minimize infections.

1.1. Motivation and Work Objectives

The main goal of this Thesis is the development of a new surface with the ability to minimize the problems of the usual materials used in dental implants regarding slow osseointegration and peri-implantitis infection. Therefore, the incorporation of silver (Ag) nanoparticles to a nanoporous tantalum oxide surface aims to increase the antibacterial properties of the implant thus reducing the risk of infection and, at the same time, promoting osseointegration capacity by chemical and morphological modification of the Tantalum surface.

Currently, there are studies regarding the biocompatibility of tantalum and the benefits of its properties in dental implant applications, as well as studies regarding the

antibacterial properties of silver. However, the amount of research that refers both studies simultaneously is very scarce, thus the need of a surface material capable of promoting osseointegration in addition to having remarkable antibacterial properties arises. So, the main objective of this dissertation is to conjugate:

- Bioactive tantalum nanoporous substrate properties;
- Antibacterial properties of silver nanoparticles;
- Controlled release of silver nanoparticles by introduction of a Carbon layer.

1.2. Dissertation Struture

The structure of this dissertation consists in 7 main chapters outlined and schematized in Figure 1.1.

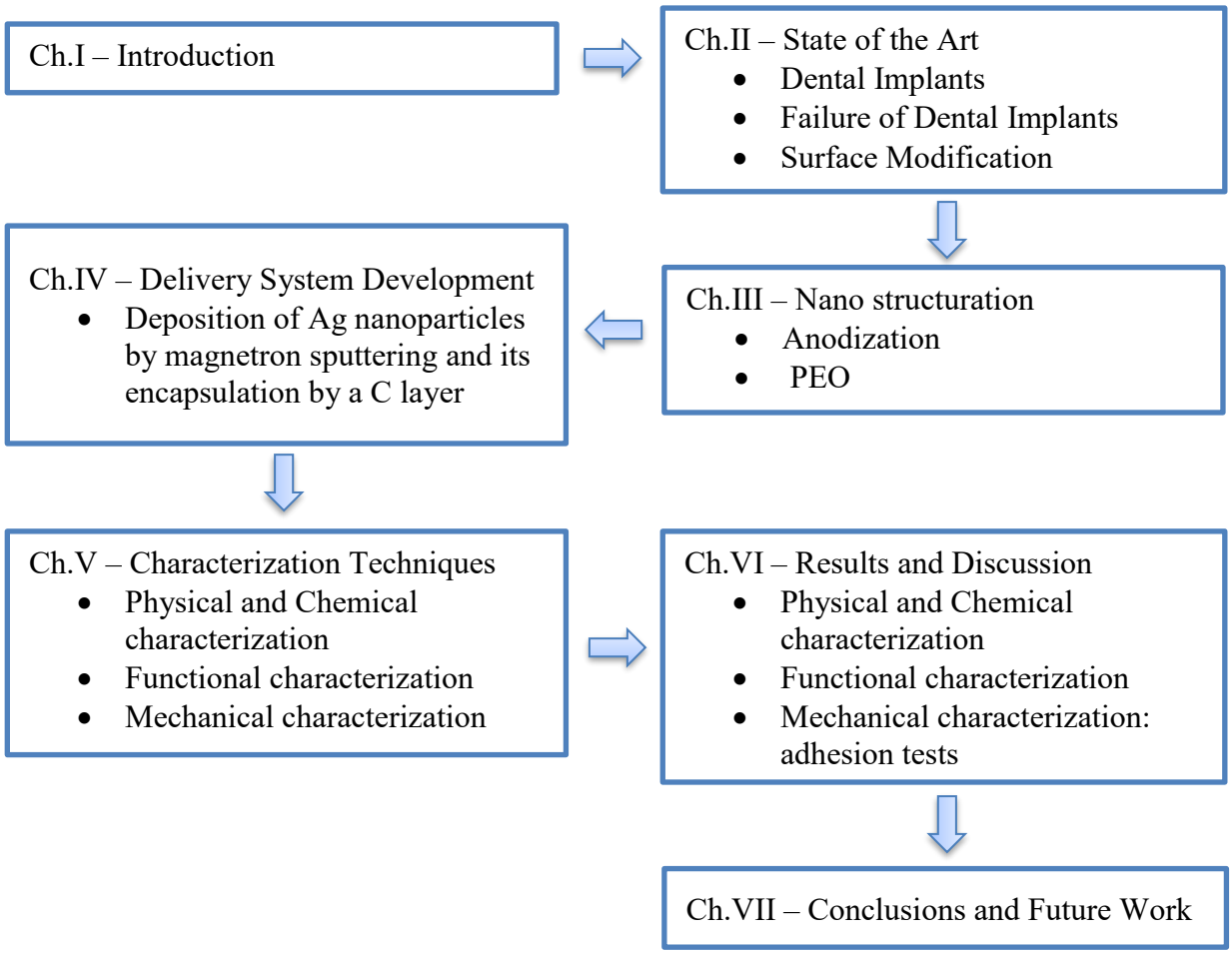

Figure 1.1. Schematized representation of thesis structure.

2. STATE OF THE ART

2.1. Dental Implants

Teeth have numerous important functions. These bone structures are used for mastication, can serve as tools, participate in speech and contribute significantly to the beauty of the owner[1]. Throughout a person's lifetime, their teeth endure continuous exposure to various chemical and physical impacts, which lead to erosion of dental hard tissues, gingival recession and other oral complications with subsequent consequences such as teeth removal[2]. Therefore the demand for dental implants has been increasing over the past decades[3].

Dental implants are devices inserted into the maxillary and/or mandibular bone through surgery that replace the lost teeth. Preferably, dental implants should be in direct contact with the bone and thus promoting osseointegration[4].

Dental implants are composed of three major components: the cylindrical screw known as implant, the abutment which connects the implant with the dental prothesis, and the custom-made crown/prothesis[5].

2.2. Failure of Dental Implants

The most important interaction that confirms the long-term clinical success of a dental implant is known as osseointegration. Osseointegration occurs when the implant fuses with the bone, allowing its anchorage to the surrounding bone tissue[6].

Most implants are successfully inserted with a survival rate rounding 98%, however long-term complications are common. The two principal reasons for the long-term failure of dental implants are mechanical stress due to osseointegration failure, and bacterial infection (Peri-implantitis)[7].

2.2.1. Osseointegration Failure

Poor osseointegration (unsuccessful growth and interaction between the bone cells and the implant) can lead to movement of the implant itself.

The normal human tooth root attaches itself to the bone through the periodontal ligament, which allows for slight movement of the tooth. In contrast, a successful implant is completely fused with the bone and presents *no mobility*.

In order to test if the implant has successfully integrated the bone a measured force or torque can be applied to the implant, if it results in no mobility the implant was a success. If an implant allows for even the slightest movement, the implant is considered a failure and therefore a complication, even if asymptomatic. The cause of this osseointegration failure is associated with micromotions that may occur during the healing phase. Therefore, slow osseointegration leads to a longer healing phase, resulting in a longer time frame where micromotions can occur, which may ultimately culminate in an unsuccessful implant[8].

2.2.2. Peri-implantitis Infection

Peri-implantitis is an irreversible infectious pathological condition that surrounds dental implants and results in progressive loss of supporting bone tissue[9]. This complication is initiated by a bacterial biofilm, which triggers the inflammation of the soft tissues and loss of bone[10].

Peri-implantitis, if not addressed in time, can lead to alarming consequences such as osseointegration failure, which may lead to eventual implant failure[11].

2.3. Bioactive Materials

Materials used in biomedical applications should have distinctive properties such as being non-toxic, non-allergic, and present corrosion resistance inside the human body. It should also possess some mechanical properties like hardness, compression strength, tensile strength, and flexural and wear resistance[14].

Bioactive materials interact with the cells of host tissue, producing an appropriate response, which leads to the desired clinical outcome. Porosity and the interconnecting porous structure of the biomaterial have an important role in supporting the penetration, proliferation, and differentiation of osteoblasts, thus promoting osseointegration. A biomaterial should aid in the formation of the bone, possess pore volume, pore interconnectivity, pore size adequate to grant the invasion of osteogenic cells and blood vessels, and have mechanical properties similar to the tissues to be regenerated[15].

The three most used types of biomaterials in dental implants are: ceramics, polymers and metals.

Ceramics are inorganic materials that can be divided into metal oxides and other compounds. Oxide ceramics are used for surgical implant devices due to their inertness to biodegradation, high strength, and physical characteristics such as color and minimal thermal and electrical conductivity. However, the low ductility and the susceptibility to bulk fracture or chipping has resulted in some limitations[16].

Polymers have lower strengths and elastic moduli when compared to the other classes of biomaterials. They are thermal and electrical insulators and show some resistance to biodegradation. When compared to bone, most polymers have lower elastic moduli, with values closer to soft tissue. This issue and the fact that polymers present low fatigue strengths can result in some problems[16].

With this in mind, metallic biomaterials possess better mechanical properties, and thus are the most used in dental implant applications. One of the metals used in dental applications was Stainless Steel due to its good mechanical properties, however poor corrosion resistance and biocompatibility led scientists to gravitate more towards titanium implants[12].

Titanium is one of the most used dental implant materials because of its chemical and biological stability. Titanium dioxide (TiO_2) also presents great properties such as good corrosion resistance and biocompatibility. However, titanium-based implants have two major flaws: its allergic effects, and its lack of bioactivity which makes it difficult to form a direct chemical bond with the surrounding bone which negatively influences bone fixation, and consequent osseointegration[17] [12].

In order to avoid the problems of titanium a sustainable alternative has been pointed: tantalum (Ta), due to its bioactivity with good biological responses. Furthermore, porous tantalum pentoxide (Ta_2O_5) shows better osteogenic outcomes when compared to porous TiO_2. In addition, tantalum presents better antibacterial performance than titanium[18].

2.3.1. Tantalum

Tantalum (Ta) is a dark-blue gray highly dense and ductile metal. This rare element is mainly obtained from tantalite-columbite ($((Fe, Mn)(Nb, Ta)_2O_6)$ [2,19]. Tantalum and its alloys retain significant mechanical properties at temperatures up to 1000°C but undergo considerable degradation due to crystal growth at higher temperatures. It is chemically stable, oxidizing in air at 300°C[20]. This combination of excellent mechanical properties lead to early consideration of Ta as a human implant material[21]. Tantalum manifests two crystalline phases with totally different properties: a stable α-phase with a body-center cubic lattice structure and a metastable β-phase with a tetragonal lattice structure. Bulk tantalum exhibits the α-phase, which presents good ductility, high melting temperature (2996°C), great mechanical properties (Hardness=8-12GPa) and low resistivity (15-80 μ Ω.cm). β-Tantalum, which has high resistivity (150-200μ Ω.cm), is brittle (Hardness=18-20GPa) and unstable above 750°C because of the transformation from β-phase to α-phase[22].

Tantalum pentoxide is the most frequent form in which tantalum binds with oxygen. Ta_2O_5 is the only acknowledged equilibrium phase. None of the other oxides (TaO_x ,TaO_y ,TaO, Ta_2O_3, TaO_2, Ta_3O_9) have been isolated in pure form, and the methods of their synthesis are not easily reproducible [23]. Tantalum oxide nanostructures display outstanding electrical and optical properties, as well as high chemical stability[24].

Figure 2.1. demonstrates the equilibrium phase diagram of the system (Ta-O). It is important to note that the Ta-phase is stable until 5 at. % of O, while the most frequent form Ta_2O_5 is only achieved for 71 at. % of O. Between these two stable phases of the diagram, there is a mixture of phases[12].

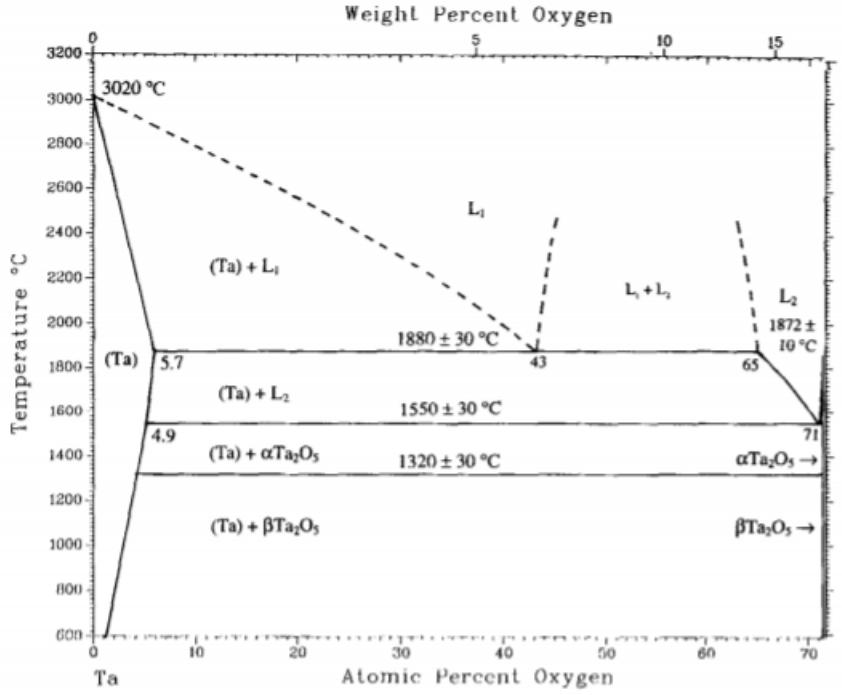

Figure 2.1. Ta-O phase diagram [2] **.**

Ta presents a favorable biocompatibility, hemocompatibility, safety and corrosion resistance. It is highly unreactive and biocompatible to the body. In addition, tantalum does not exhibit toxicity to surrounding cells, nor does it inhibit local cell growth of surrounding bone. Therefore, tantalum has been adopted to manufacture biomedical implants used for orthopedic, dental, and craniofacial surgeries in clinical practice. With this in mind, many articles have been written by investigators describing and studying the properties of Ta and Ta_2O_5. Numerous studies report that a tantalum thin film has been used to coat titanium samples improving its chemical stability, optical properties, biocompatibility and corrosion resistance[25].

Huang *et al.*[25], demonstrated that the deposition of a tantalum oxide (Ta_2O_5) layer on a Ti sample enhanced the antibacterial properties against *S. aureus* and *A. Actinomycetemcomitans*. Moreover, the ISO-10993-5 cytotoxicity test proved that the Ta_2O_5 sample did not exhibit cytotoxic effects in soft and hard tissues.

2.3.2. Hydroxyapatite

Calcium phosphate (CaP) ceramics, more precisely hydroxyapatite (HA) has been used as an implant coating material, particularly in dentistry due to its excellent biocompatibility properties[26].

CaP has been the subject of extensive research because of its biocompatibility and mineral chemistry, which resembles those of human bone. CaP has been widely applied to metallic implants, such as titanium implants as a coating material. HA-coated implants promote faster healing and bone attachment when compared to noncoated implants. These coated implants also show better clinical results when implanted in areas with poor bone quality[26].

HA-coatings were proved to possess biological advantages, including the enhancement of bone formation and faster bonding between the implant surface and the surrounding bone[26].

As it can be seen in Figure 2.2. coating titanium implants with CaP increase the surface area, biocompatibility, and osseoconductive effect which promotes cellular activity, thereby enhancing osseointegration[26].

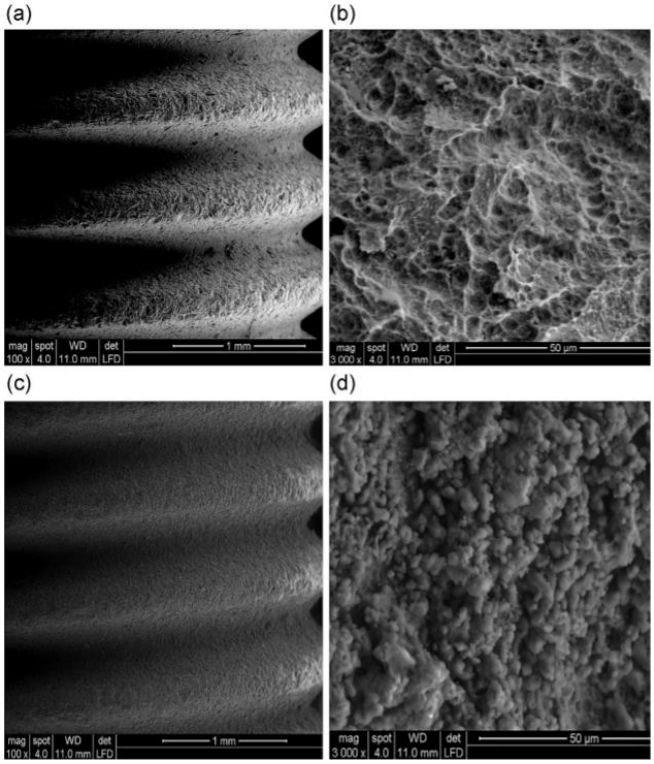

Figure 2.2. (a) Titanium Implant, (b) Scanning electron microscope (SEM) image of titanium implant before coating, (c) Titanium implant with HA coating, (d) SEM image of titanium implant with HA [26].

2.4. Surface Modification

Surface Modification can improve the interaction between the surface and the adjacent tissues, consequently reducing inflammatory responses and possible infections[12]. Furthermore, implant surface treatment aims to modify surface topography and chemistry and consequently its surface energy, in order to promote bone cell proliferation and differentiation, thus accelerating osseointegration[13].

Osseointegration is the direct functional and structural connection between the living bone tissue and the surface of the implant. Osseointegration is a very important parameter to study when evaluating an implant's success in terms of healing and longevity[13].

Surface topography has a valid effect on the implant's success and can improve osseointegration overtime, as well as reducing healing time[13]. It has been confirmed that producing pores with nanometric dimensions results in a greater interaction between proteins, ion and biomolecules, resulting in the proliferation of osteoblasts and, thus promoting osseointegration[12].

Processes such as anodization are used to manipulate surface topography and chemical properties. Commonly anodized surface implants undergo electrolyte and current treatment by being placed as the anodes of galvanic cells with the electrolyte. This anodic oxidation promotes the growth of a layer with a porous topography, developing a rough surface. An *in-vivo* study with anodized titanium implants proved that the anodized surfaces had a biocompatibility similar to hydroxyapatite-coated surface implants[13].

This electrolytic process can be modified by using a solution containing nanoparticles in a mixture of phosphoric acid and calcium nitrite as the electrolyte. By miming the composition of hydroxyapatite, which is a mineral present in the bone composition, osseointegration is accelerated[13].

Another problem regarding dental implants is the adhesion of bacteria to the implant. In order to solve this issue bactericidal surfaces capable of killing bacteria have been developed[12]. Processes such as sputtering allow to modify the surface by nanoparticle deposition onto the implant surface. Ag, Cu and Zn nanoparticles and its oxides such as AgO, CuO and ZnO prevent initial bacterial attachment and therefore biofilm formation, ultimately preventing infections[12].

2.5. Antimicrobial Activity of Nanoparticles

A nanoparticle can be defined as an object of very small dimensions "that behaves as a whole unit in terms of its properties".[27] Nanoparticles have amongst them various important characteristics that can be used to classify them such as composition, morphology, uniformity, and agglomeration. Additionally, nanoparticles are classified according to their diameter size[27]. Their size ranges from 1 nanometer to 100 nanometers and can correspond to individual molecules or macromolecules which include higher-order assemblies into nanoparticles[28].

Nanoparticle size allows different biological interactions when compared to non-nanostructured materials due to the surface to volume ratio. This distinct interaction can be exploited to create nanostructures capable of diagnosing and treating numerous pathologies[29]. Taking this in consideration, NP degradation (breaking down nanoparticles to smaller order assemblies such as atoms, clusters and molecules) is being considered as a drug release application, avoiding long-term accumulation inside living subjects, thereby having a beneficial impact on the biocompatibility of NPs[30].

Regarding nanoparticulate metals, the antimicrobial properties of silver (Ag) and copper (Cu) have been extensively studied by incorporating both into various test substrates. The results of these studies revealed an inverse relationship between the size of nanoparticles and antimicrobial activity. Particles in the size range of 1-10 nanometers proved to be the most effective at killing the bacteria. However, it was reported that smaller nanoparticles of silver are more toxic than larger ones, and the toxicity is even higher when in oxide state. In the specific case of silver NPs, Ag^+ ions are released from the surface acting as an antibacterial agent[31].

Even though silver nanoparticles have very effective a*ntibiotic* effects against a broad variety of bacteria, its free ionic form was also proven to be toxic to human cells. Tests regarding the antibacterial applications of silver nanoparticles revealed that layering these particles on oxidized metal substrates can lessen their toxicity towards humans. Consequently, the most recent major breakthroughs for increasing the antibacterial activity of implants relate to the combination of silver NPs with oxides, such as TiO_2 and ZnO[32]. This fact can be atributed to TiO_2 and ZnO metal oxide semiconductor nanoparticles ability to destroy bacteria by ROS mechanism while under UV light. It occurs when a photon of higher energy than their optical band gap is absorbed by these nanoparticles. The electron-

hole pairs are created and generate ROS. Due to the wide band gap of these nanoparticles only a light source in the UV radiation range could be used for their activation[32].

2.5.1. Silver Nanoparticles

Silver is a transition metal which distinguishes itself by having the highest electrical and thermal conductivities of all metals, as well as a very high reflectivity and a low emissivity. This metal is also characterized by having only one crystal form, a face-centered cubic arrangement with a lattice constant of a = 0.4086 nm, as is presented in Figure 2.3[33].

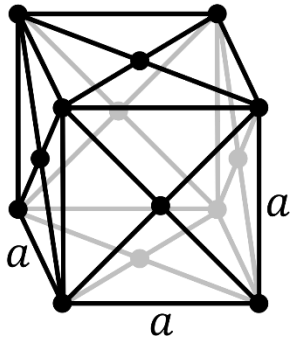

Figure 2.3. Ag unit cell structure.

Ag is currently used as an antibacterial agent with multiple applications. It has been previously proven that metallic silver is highly active in killing bacteria, therefore Ag NPs have recently attracted considerable attention of researchers in different fields such as catalysis, optoelectronics, biomedicine, wound dressing, biomedical devices, and food preservation[34].

Silver nanoparticles have high surface to volume ratios with different morphological features. These important characteristics mean that silver NPs can easily penetrate the bacterial cell membrane and work as a catalyst to destroy the bacterial cell through various different processes. However, it is also reported that an imprudent and/or excessive usage of silver NPs can result in potential risks to humans and the environment. Thus, it is crucial to maintain the concentration of free Ag NPs below the permissible limits set by WHO (World Health Organization)[34].

2.5.1.1. Silver Antibacterial Mechanisms

The definition of antibacterial activity, as stated by The Miller-Keane Encyclopedia and Dictionary of Medicine, Nursing and Allied Health 2003, is known as the action by which an agent is able to destroy or suppress the growth or reproduction of bacteria. Several mechanisms which silver nanoparticles employ to cause antimicrobial effect have been pointed and studied. These mechanisms are: (i) release of Ag^+ which reacts with thiol groups of proteins and interfere with DNA replication, (ii) generation of free radicals which damages the bacterial membrane and (iii) direct physical contact between the nanoparticles and bacterial cells which causes structural damage to their wall [35].

2.5.1.1.1. Release of Silver Ions

Sukumaran *et al.*[36], proposes that the silver ions released by the nanoparticles can interact with the thiol groups of many vital enzymes and inactivate them. The contact between bacterial cells and silver causes the cell to take in silver ions which suppress several functions in the cell, subsequently damaging them. This triggers the generation of reactive oxygen species (ROS), which are perhaps produced through the inhibition of a respiratory enzyme by silver ions and attack the cell.

The author also reported that silver, being a soft acid, has a natural tendency to react with a soft base. Therefore, since cells are majorly made up of soft bases such as sulfur and phosphorus, the presence of silver ions generates ROS and leads to cell death. Considering that DNA also has sulfur and phosphorus-based components it is logical that AgNPs will also react with these soft bases destroying the DNA and eventually leading to cell death. This interaction can also lead to problems in DNA replication of the bacteria and result in the termination of microbes[36]. The whole process is synthesized in Figure 2.4.

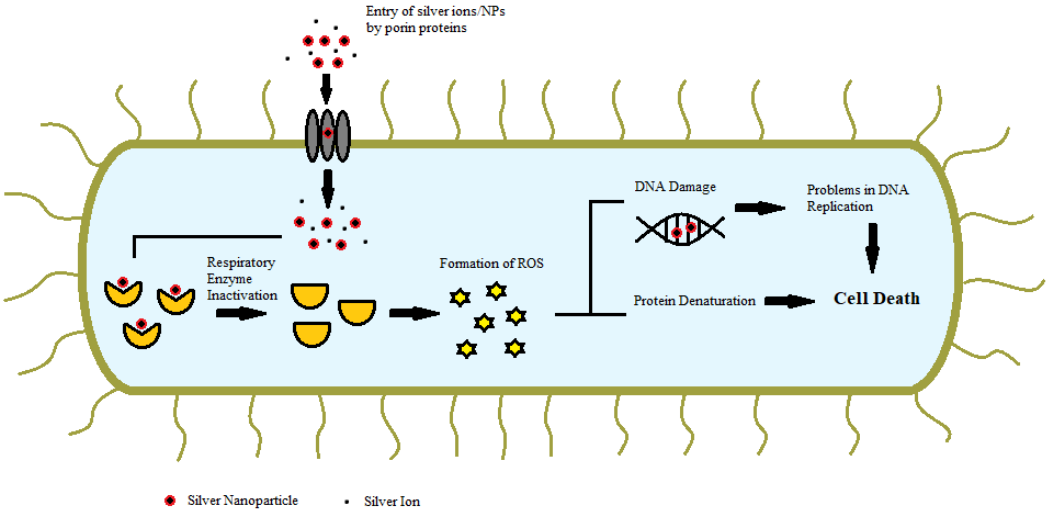

Figure 2.4. Release of Silver ions as an antibacterial mechanism.

2.5.1.1.2. Generation of Free Radicals

An alternative mechanism that may cause cell death is the formation of free radicals by the silver NPs and their interaction with the bacterial cell. Electron spin resonance spectroscopy studies indicate that silver nanoparticles generate free radicals when in contact with the bacteria. These free radicals can damage the cell membrane and make it porous which can eventually result in cell death, as seen in Figure 2.5[36].

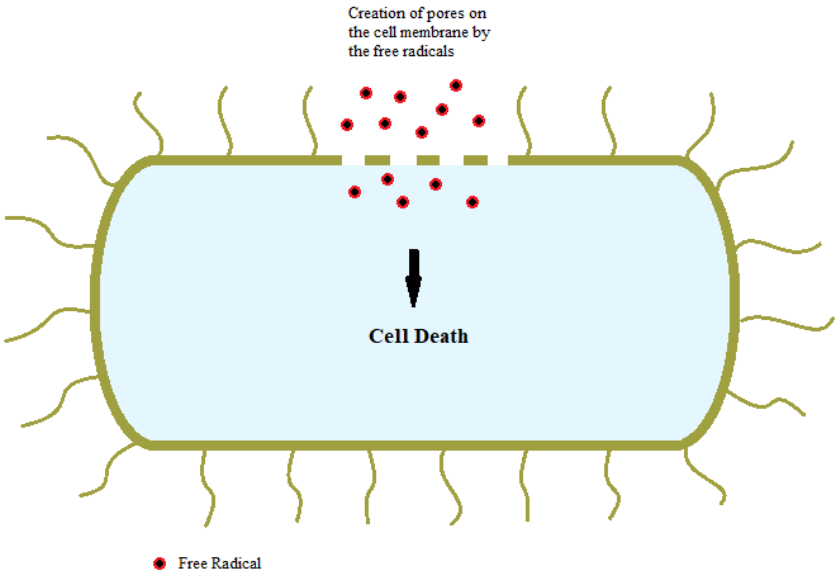

Figure 2.5. Generation of free radicals as an antibacterial mechanism.

2.5.1.1.3. Direct Physical Contact

The third mechanism relies on the ability of the silver nanoparticles to anchor themselves to the bacterial cell wall and subsequently penetrate it, thereby causing structural changes in the cell membrane and ultimately resulting in the death of the cell. This behavior is schematized in Figure 2.6[36].

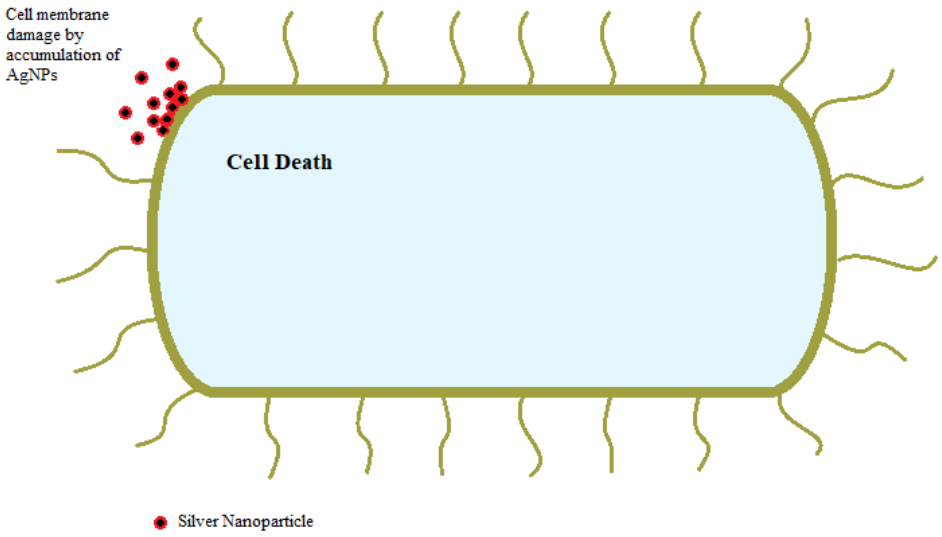

Figure 2.6. Direct physical contact as an antibacterial mechanism.

3. BIOACTIVE NANOSTRUCTURED SURFACE

In this chapter it is presented a description of the surface modification techniques used to obtain the final tantalum oxide nanostructured surface, in order to improve its chemical and physical properties.

3.1. Anodization

Anodization is an electrochemical technique extensively used for the preparation of metal oxides due to its relatively low price, good controllability, high repeatability and simple operation[3738].

During the anodization process, a voltage (10-80V) is applied between a cathode and the metallic substrate (anode) immersed in an electrolytic solution.

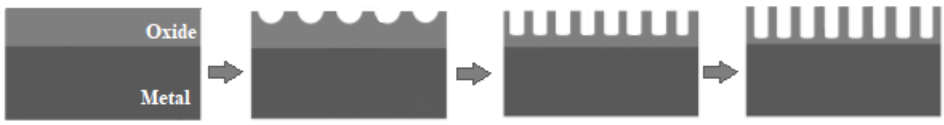

Figure 3.1. Development of an oxide porous columnar structure through anodization. Adapted from [12].

During the exposure to the anodic voltage an oxidation reaction will occur at the substrate surface (Figure 3.1). There, the following reaction takes place : $M \rightarrow M^{n+} + ne^{-}$ (M as symbol of the metal) and the M^{n+} ions will move towards the surface of the substrate. Simultaneously, O^{2-} ions provided by the H_2O present in the electrolyte migrate towards the metal substrate, and at its surface O^{2-} will react with the M^{n+} ions to create a metal oxide layer (MO_x)[39].

Throughout the formation of the oxide metal layer pores are formed through two main processes: Electric Field Dissolution and the Breakdown Process[12].

Electric Field Dissolution is a mechanism of pore creation composed of three distinct phases (Figure 3.2). The first phase consists in the previously described metal oxide layer formation. This phase is followed by a localized dissolution of the oxide layer due to the F^- ions that have to be present in the electrolyte, therefore resulting in the formation of small irregular pores, known as pits. When these pits are formed the electric field intensifies at the pore bottom therefore enhancing the dissolution rate of the oxide layer, which causes the small pits to grow into nanopores, putting an end to phase two. The third phase concludes with the matching between the oxide layer dissolution and the oxide layer creation rates at the pore/electrolyte interface. Thus, the thickness of the oxide layer remains the same, although it moves further into the metal increasing the pore depth. Figure 3.2 is a schematic representation of this mechanism[12].

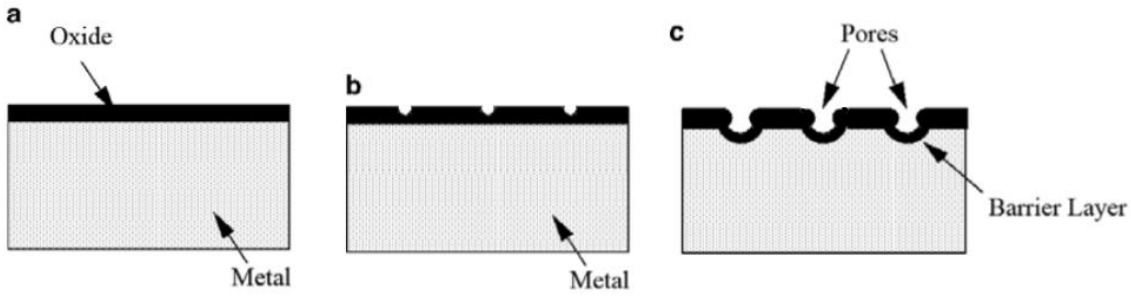

Figure 3.2. Schematic representation of the Electric Field Dissolution Mechanism. a) Phase1, b) Phase 2, c) Phase 3. Adapted from [40] .

The breakdown mechanism consists in anodizing by using a potential above the breakdown limit. The high potential generates an electrical field capable of breaking the oxide and collapsing the anodized layer, and therefore creating pores. The potential needed to achieve this mechanism varies depending on the anodized metal and the electrolyte[12].

3.2. Plasma Eletroctrolytic Oxidation

Plasma Electrolytic Oxidation (PEO), also known as Microarc Oxidation (MAO), is an efficient electrochemical process capable of forming a porous oxide film on top of a substrate. Simultaneously, this technique allows the incorporation of bioactive elements such as calcium (Ca) and phosphorus (P), in order to facilitate the osseointegration process[41]. Hence, this surface modification strategy has been heavily used in orthopedic and dental applications. It is also important to mention that the PEO process parameters such as:

electrolyte composition, current intensity, temperature, process time and applied voltage can be changed in order to obtain a specific coating[42].

PEO process is an aqueous anodic treatment. As in the anodization process a metal substrate is submerged in an electrolytic solution as the anode. The main difference is that in PEO treatment a higher voltage (~250-800V) courses through both the anode and cathode to trigger a discharge arc at the substrate/electrolyte interface. Since PEO occurs at a higher voltage it triggers gas and plasma emission, and consequently porous surface morphologies with high levels of pore interconnectivity are created[42].

This technique uses a positive potential above the electrolytic breakdown voltage value of the oxide layer, forming a coating capable of incorporating elements of the electrolyte and metal. The oxide layer created using this process presents important properties for dental applications such as high corrosion resistance, good hardness, high adhesion strength and high economic efficiency. Finally, it is also described that the incorporation of hydroxyapatite in the coating, through PEO, enhances the sample's bioactivity and biocompatibility[42].

3.2.1. PEO Mechanism

The PEO process under galvanostatic conditions presents three different stages that varies with the evolution of the voltage. In the first stage, similarly to the traditional anodization, the voltage increases linearly with the oxidation time. The second stage starts when the voltage value exceeds the dielectric breakdown limit of the oxide layer. At this stage microarc discharges start to occur and the voltage increases at a slower rate. In the final stage the voltage achieves a rather stable value, with slight fluctuations. For the remainder of the oxidation time the spark size increases, and an association between the fluctuations and the continuous breakdown and formation of the oxide layer can be made. Figure 3.3 is a graphical representation of the different stages that occur in the PEO process.

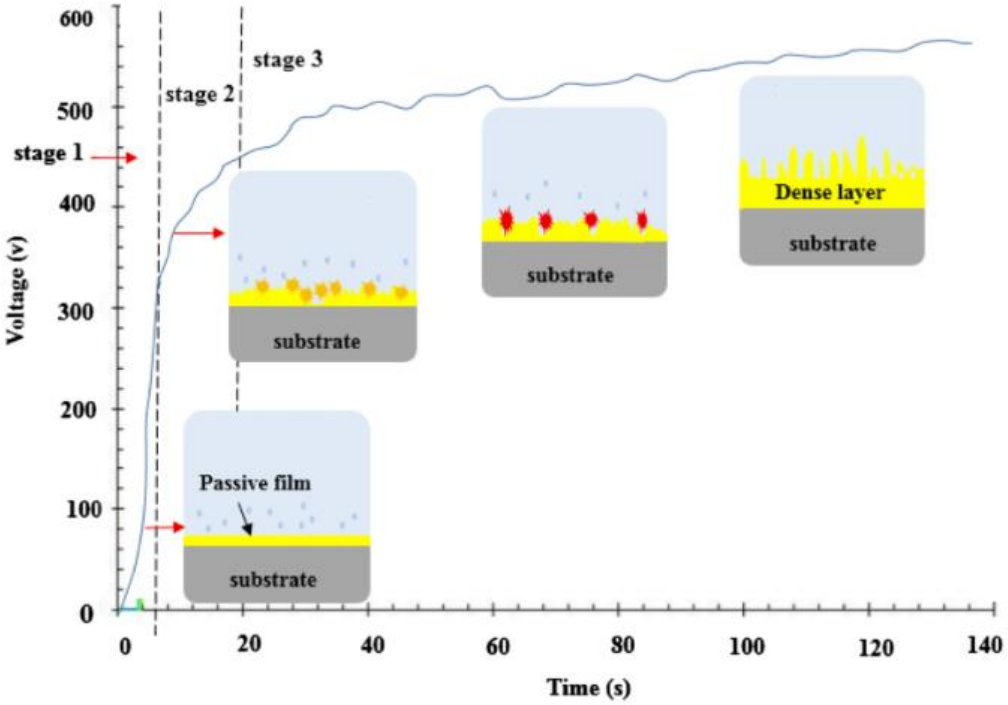

Figure 3.3. Graphical representation of the cell potential (V) vs time (s). Curve representation for the three stages of PEO coating on a metal substrate (Niobium). Adapted from [43].

3.3. Tantalum Plasma Electrolytic Oxidation

High-pure Tantalum sheet (Ta Sheet T1-9000-D70, 99.95% purity, Testbourn Ltd) was cut into 3x1x0.5 mm^3 substrates. Previous to the PEO treatment each Ta sample was cleaned using an ultrasound machine. Firstly, all the samples were ultrasonically cleaned in ethanol for 5 minutes, followed by 5 minutes in distilled water. This ultrasound cleaning process prevents the presence of impurities on the sample. Each cleaned Ta substrate was then placed in an electrochemical cell, as it can be seen in Figure 3.4(a). In this picture is also present the cathode (graphite) (Figure 3.4(b)), which was placed 30 mm away from the sample. The presence of a small agitator (Figure 3.4(c)) can also be observed, the purpose of this tool is to mix the electrolyte in order to enhance the ion interaction between the sample and the electrolyte and consequently facilitate the formation of an oxide layer.

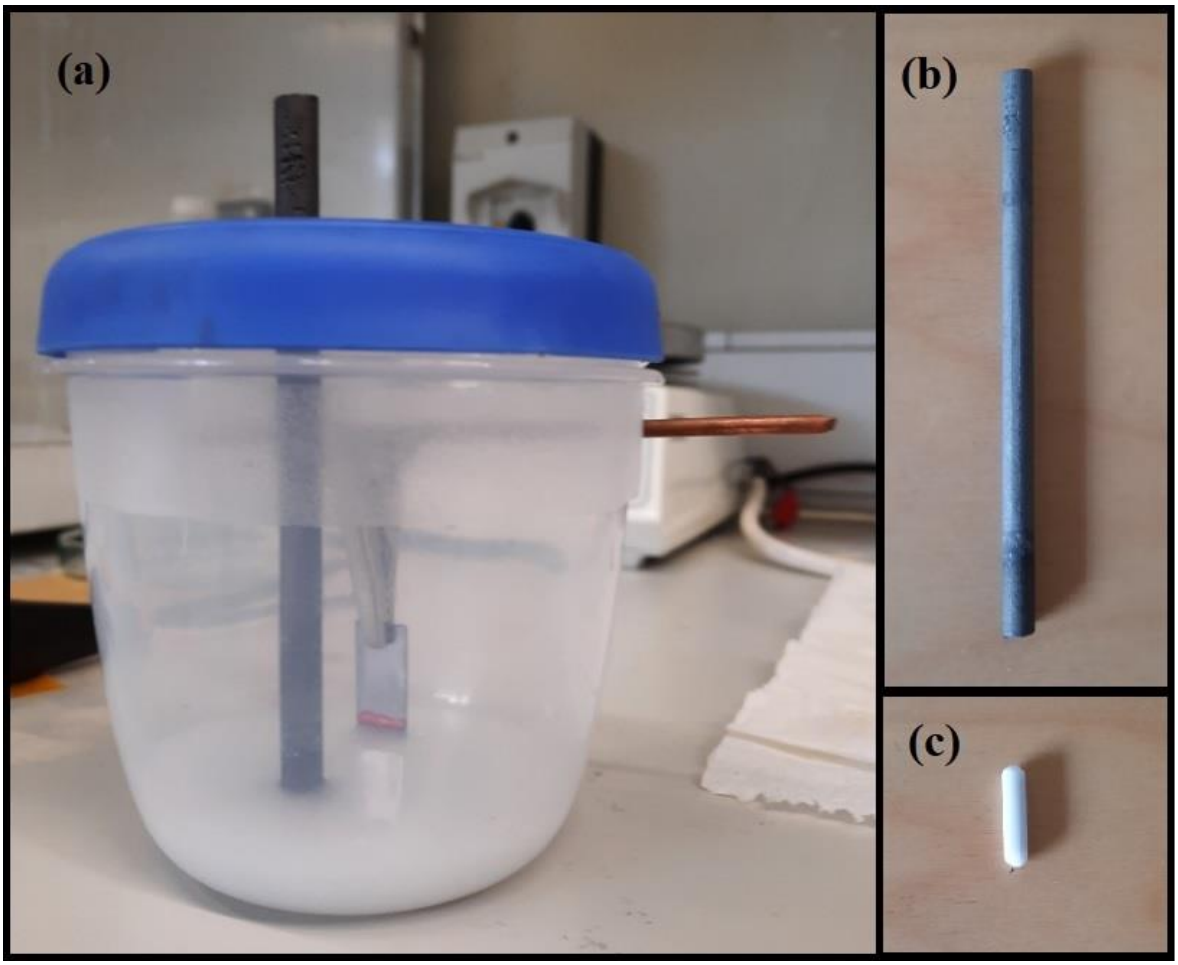

Figure 3.4. (a) Electrochemical Cell, (b) Graphite Cathode, (c) Agitator .

When all the components were in position 50 mL of electrolyte were placed inside the electrochemical cell to cover an area of 1x1.2 mm^2 of the substrate. According to Fialho *et al.*[18] results, for the purpose of obtaining a Ca/P ratio appropriate to promote osseointegration the electrolyte was composed of 0.35 Molar of calcium acetate (99% purity, Biochem Chemopharma) and 0.12 Molar of β-Glycerophosphoric Acid Disodium Salt Pentahydrate (98% purity, Acros Organics). To achieve the adequate ratio of calcium and phosphate the exact mass of each reagent was calculated using the Molarity Equation:

$$\text{Molares} = \frac{\frac{\text{m(g)}}{\text{M}(\frac{\text{g}}{\text{mol}})}}{\text{L(L)}}$$

Since the electrolyte was prepared in batches of 150 mL and the molar mass of calcium acetate and β-Glycerophosphoric Acid were 158.17 g/mol and 306.11 g/mol respectively, the mass of each reagent was the following:

Calcium Acetate:

$$0.35 = \frac{\frac{m(g)}{158.17(\frac{g}{mol})}}{150x10^{-3}(L)} \equiv m = 8.30\ g$$

β-Glycerophosphoric Acid:

$$0.12 = \frac{\frac{m(g)}{306.11(\frac{g}{mol})}}{150x10^{-3}(L)} \equiv m = 5.51\ g$$

Previous work also mentions that to achieve a nanoporous tantalum oxide layer through PEO, a potentiostatic voltage of 200 V needs to be applied for 30 minutes, with an electric current of 3 A, at room temperature[18].

With the intention of mimicking those experimental parameters an EA-EL 9000 B Power Supply was used, and the final PEO treatment system can be observed in Figure 3.5.

Figure 3.5. PEO Treatment System.

After the PEO process finished each sample was cleaned in distilled water, dried and the oxidized part was cut into 1x1 mm^2 squares.

4. NANOPARTICLE AND CARBON LAYER DEPOSITION

In this chapter it is presented the method chosen to deposit the silver nanoparticles, as well as the thin film of carbon, on top of the manufactured tantalum substrate (with incorporated NPs). Furthermore, it also documents the parameters chosen for each deposition.

4.1. Magnetron Sputtering

Magnetron Sputtering is a physical vapor deposition (PVD) technique with the ability to create thin films.

Sputtering methods start with the creation of plasma through the application of an electrical field to a neutral gas (Argon in this thesis) in a low vacuum environment. The electrical field results in the excitation of the electrons and ions from the neutral gas, guaranteeing its ionization. The ionization is followed by collisions between these ions and the target material, consequently removing atoms and secondary electrons from the target. Finally, the removed target ions condensate onto the substrate.

Magnetron Sputtering uses a magnetic field to force the ions movement in target proximity, multiplying the probability of collisions between ions and atoms. This method increases the deposition rate and simultaneously lowers the target heating. It is also possible to be operated at low pressures and voltages[35].

4.1.1. Deposition of Ag nanoparticles

Firstly, several depositions onto Silicon TEM grids were made to gather information about the desired nanoparticle size and its deposition time. The results of this deposition ([APPENDIX A]) showed that the optimal sizes for the nanoparticles were 1nm and 2nm since bigger NPs did not maintain their individuality.

Silver nanoparticles were then deposited onto the previously produced tantalum oxide substrates in a dual magnetron sputtering chamber. Each magnetron was connected to a power supply and equipped with a silver target with the following dimensions: 200x100x10 mm^3. An octagonal substrate holder was placed at the center of the chamber

12 cm apart from both targets. The system was connected to a primary rotatory pump (Pfeiffer Vacuum DUO 20 M, pumping speed 20 m^3/h) to supply the primary vacuum and a secondary diffusion pump (BOC Edwards Diffstak 160/700, pumping speed 760 l/s) to achieve a secondary vacuum with the pressure inside the chamber reaching around $4.0x10^{-4}$ Pa. This double vacuum procedure minimizes the contact between the substrate holder and the environment, thus diminishing target oxidation. Therefore, the substrate holder was placed for 15 minutes in the chamber with the primary pump functioning. The magnetron sputtering system is represented in Figure 4.1.

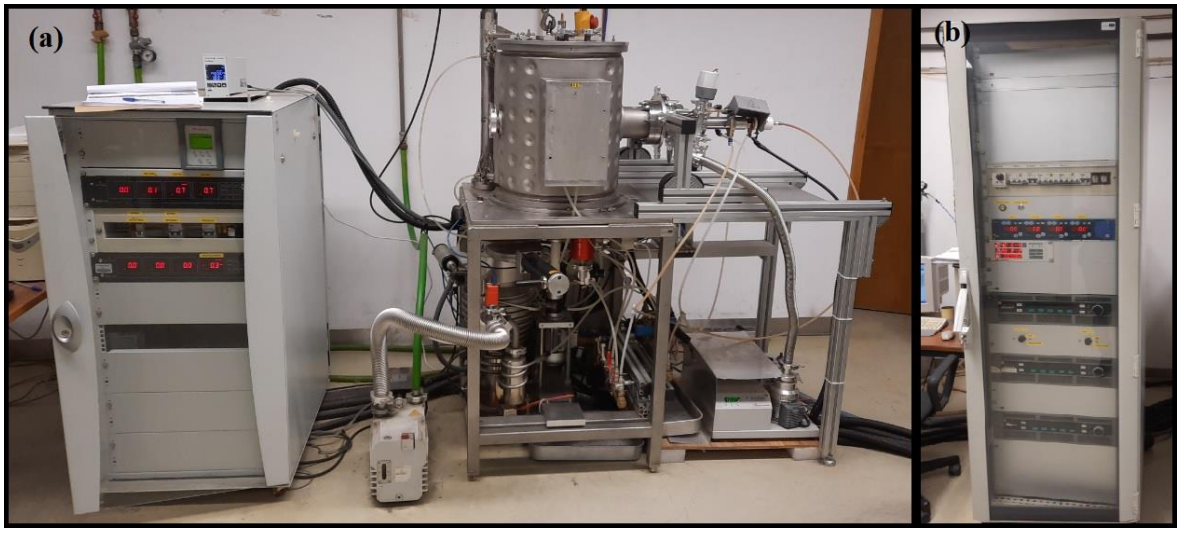

Figure 4.1. (a) Magnetron Sputtering Machine, (b) Power Supply .

The nanoparticles were formed in an Argon (Ar) atmosphere (30 sccm), using one pure silver (99.99%, Testbourn Ltd) target connected to a DC-pulsed power supply (Advanced Energy Pinnacle Plus). The chosen gas was Argon, due to its inert nature, which implies it will not provoke a reaction with the deposited material. Its compatibility with most materials used in sputtering also translates in a more efficient energy transfer.

Previous to the depositions the substrates were cleaned in an ultrasonic bath in Acetone for 10 minutes and Ethanol for 10 minutes, to prevent contamination, and remove impurities.

Based on the previous work two different Ag NPs sizes were deposited onto the Ta nanostructured substrate: 1nm and 2nm. All the important parameters used to create both silver NPs sizes are presented in Table 4.1, where the deposition time should be highlighted.

Nanoparticle Size	Base Pressure (Pa)	Work Pressure (Pa)	Deposition Time (s)	Power Density (W/m^2)	Current Density (A/m^2)	Voltage (V)
1nm Ag	$4.1x10^{-4}$	0.28	5	5000	11.5	427
2nm Ag	$4.2x10^{-4}$	0.27	10	5000	11.5	427

Table 4.1. Silver nanoparticles deposition parameters.

4.1.2. Deposition of Ag nanoparticles covered with a Carbon Film.

In this case, opposed to the sole deposition of the silver nanoparticles based on the TEM deposition, optimization of the carbon film was a necessary step, which is described in ANNEX A.

After the optimization process, the goal was to replicate the same two depositions described in the last subchapter, subsequently covering them with a thin carbon layer with a thickness of around 4 nm. Therefore, the same dual magnetron sputtering chamber was used, this time with a magnetron connected to a silver target and the other to a carbon (99.99%, Testbourn Ltd) target with the following dimensions: 200x100x10 mm^3.

Firstly, the 1 nm Ag nanoparticle deposition was replicated, with only the magnetron connected to the Ag target turned on, and a shutter covering the C target. Afterwards, the magnetron connected to the Ag target was turned off and the shutter was moved in front of the silver target. Then, the magnetron connected to the carbon target was turned on for 55 seconds to deposit the thin carbon layer on top of the nanoparticles.

Later, the process was repeated to deposit the thin carbon film on top of the 2nm sized silver nanoparticles. All the values recorded in both depositions are presented in Table 4.2 andTable 4.3.

Nanoparticle Size	Base Pressure (Pa)	Work Pressure (Pa)	Deposition Time - Ag (s)	Power Density - Ag (W/m^2)	Current Density - Ag (A/m^2)	Voltage Ag (V)
1nm Ag + C	$4.0x10^{-4}$	0.28	5	5000	11.5	427
2nm Ag + C	$3.9x10^{-4}$	0.26	10	5000	11.5	427

Table 4.2. Silver nanoparticles and carbon film deposition parameters.

Nanoparticle Size	Base Pressure (Pa)	Work Pressure (Pa)	Deposition Time - C (s)	Power Density - C (W/m^2)	Current Density - C (A/m^2)	Voltage C (V)
1nm Ag + C	$4.0x10^{-4}$	0.28	55	60000	92.5	646
2nm Ag + C	$3.9x10^{-4}$	0.26	55	60000	92.5	646

Table 4.3. Silver nanoparticles and carbon film deposition parameters.

5. CHARACTERIZATION TECHNIQUES

5.1. Physical and Chemical Characterization

Physical and chemical characterization techniques were used with the objective of evaluating the morphology, topography, elemental composition, and crystalline structure of the tantalum oxide nanostructured surface with silver nanoparticles.

5.1.1. Morphology

The morphological characterization of the developed samples was obtained using scanning electron microscopy (SEM). SEM is an electron microscopic technique capable of providing an image of the sample's surface using a focused energetic electron beam. This technique is one of the most extensively used tool to study the surface morphology and identify small areas that cannot be observed by optical microscopy, such as the nanopores obtained by the plasma electrolytic oxidation technique and the sputtered silver nanoparticles[44].

SEM is an important technique for the analysis of surfaces that can withstand exposure to vacuum. If the surface is not conductive the SEM technique starts by sputtering the surface with a thin layer of metal, this makes the surface conductive, which is a requirement[45]. When this requirement is met, ions start to be generated by either thermionic guns or field emission guns and are then focused by a series of electromagnetic lenses. The electron beams then hit the sample's surface which emits X-rays and three kinds of electrons: primary backscattered electrons, secondary electrons, and Auger electrons. In this technique only primary backscattering electrons and secondary electrons are collected by an appropriate detector and used to generate images of the sample[45] [46]. This process is schematized in Figure 5.1.

In this thesis, the morphology and chemical composition of the samples were evaluated using a FEI Nova 2000 scanning electron microscope (SEM) by secondary electron and at working distance of 5mm.

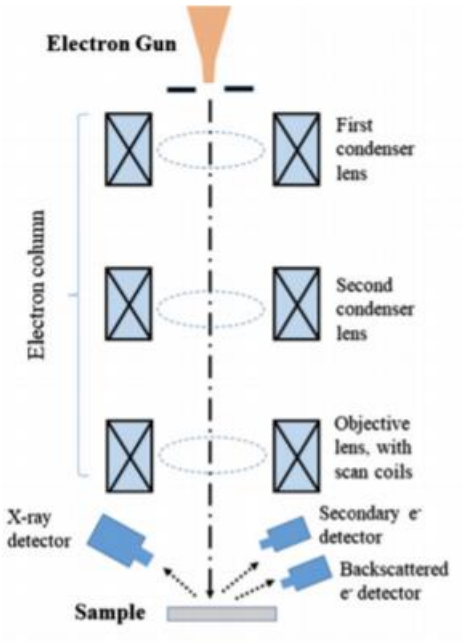

Figure 5.1. Schematized representation of the SEM technique. Adapted from [47].

5.1.2. Topography

The topographic characterization of the developed samples was performed by Atomic Force Microscopy (AFM).

Despite being a relatively recent technique, AFM has become an essential mechanism for nanoscale surface imaging. Regarding biomaterials, AFM possesses some advantages when compared to other imaging techniques. Firstly, sample preparation is simpler for AFM in comparison to SEM. AFM is also capable of producing detailed three-dimensional maps instead of two-dimensional images without expensive and prolonged sample preparation[44].

In AFM imaging, the sample is scanned line-by-line using a sharp probe tip mounted on a micro-cantilever, thus generating a topographic image of the surface. The interaction between the tip and the surface causes the cantilever to deflect. This deflection is monitored by a laser that is focused on the top of the cantilever, and from there is reflected onto a split photodiode. When the laser spot moves on the photodiode it triggers an electric signal change that is used in a feedback loop in order to maintain the exerted force constant. During the feedback loop, voltage is applied to a piezoelectric scanner, which moves either the tip or the sample up and down. This vertical movement of the piezo enables the

generation of an image of the surface's topography[48]. A schematic diagram of a typical AFM instrument is depicted in Figure 5.2.

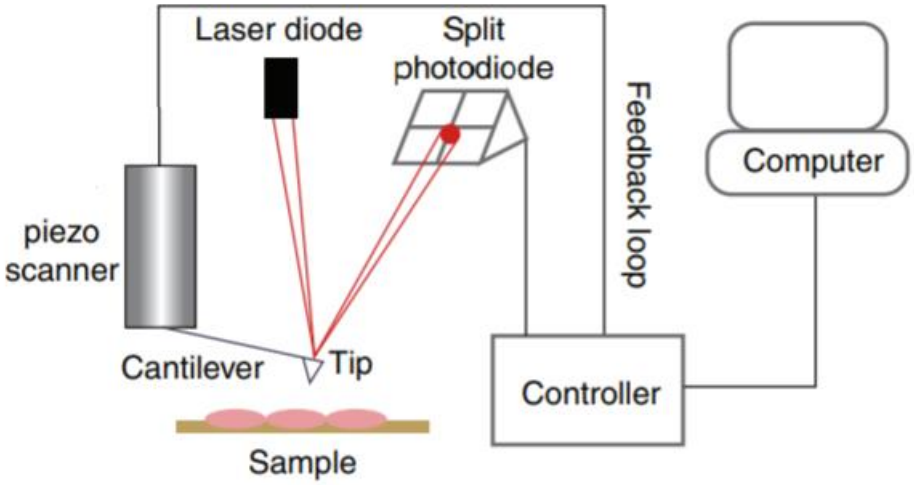

Figure 5.2. Sketch illustrating the principal of Atomic Force Microscopy. Adapted from[48].

There are three operating modes of AFM: contact mode, non-contact mode, and tapping mode. In this work it was used the tapping mode to analyze the topography of the samples. This mode is the most suited for the characterization of biomaterials since, although there is still mechanical contact, damage to the sample's surface is lessened as the contact is intermittent and no lateral force is applied to the sample[44].

In the tapping mode, a vibrating micro-cantilever is held at tip-to-sample distance. During the vibrational movement the cantilever's lowest point taps the surface. While the cantilever vibrates, the sample is dragged beneath the tip which leads to changes in the cantilever's vibrational parameters. These changes are monitored and the feedback correctional parameters are used to keep the vibration constant and then processed to produce a topographical image[49].

In this thesis, the surface topography and roughness were assessed by atomic force microscopy (AFM) (Bruker di Innova) with a conductive Si cantilever in tapping mode, the RTESP-300 probe from Bruker, (8nm radius of curvature). The average roughness (Ra) was obtained in a $10x10\mu m^2$ area.

5.1.3. Chemical Composition

The composition characterization was performed by Energy Dispersive X-ray Spectroscopy (EDS).

Normally, SEM is equipped with an Energy Dispersive X-ray Spectroscopy (EDS) detector with the purpose of chemically characterizing the chemical composition of each sample. This technique is based on the detection and investigation of the characteristic X-rays produced by the primary electrons, which were already mentioned in the Morphology subchapter. While electron illumination occurs, an electron in the inner-shell of the target atom can be ejected and, subsequently, an electron hole is created. Afterwards, an electron from an outer-shell occupies the hole, and the dissimilarity of energy between the outer and inner-shell electrons is released in the form of X-rays, as seen in Figure 5.3.[44]

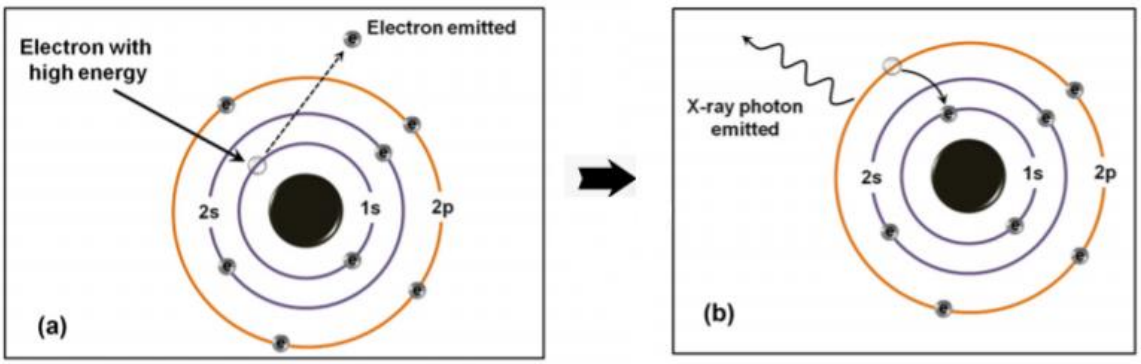

Figure 5.3. Schematic diagram illustrating the primary electron emission process. (a) High-Energy induces target atom with an inner-shell emission. (b) An electron drops from a higher energy level to the vacant hole by emitting X-rays. Adapted from[44].

This emitted X-ray has the characteristic energy of the atomic structure of the element from which it was emitted. Therefore, by measuring the quantity and energy of the X-rays emitted from the sample, it is possible to determine its chemical composition.[44]

In this thesis, the chemical composition of the samples were evaluated using a FEI Nova 2000 scanning electron microscope equipped with an EDAX Pegasus X4M detector for energy-dispersive X-ray spectroscopy (EDS) at 10 kV and at working distance of 5mm.

5.1.4. Crystalline Structures

The structural characterization of the samples was performed by X-Ray Diffraction Microscopy (XRD). This technique made it possible to identify the crystalline structures present in the tantalum oxide nanostructured samples with silver nanoparticles.

XRD is the main technique used for determining the phase of a crystalline material. Firstly, this technique starts by pointing an accelerated X-ray at the sample. From the interaction between this X-ray and the metallic sample a fraction (~1%) of this beam is converted into X-ray, while the remainder of the beam dissipates as heat. The generated x-rays produce two kinds of radiation spectrums. In the first place, x-rays without any specific wavelengths, but with a continuous spectra, are created. These spectrums are generally not used for the characterization. The second type of spectrums created are known as the characteristic spectra, which are produced by specific electronic transitions within the individual atoms of the metallic sample.

Using Bragg's law:

$$n\lambda = 2d\sin(\theta),$$

it is possible to find a relation between the wavelengths of the characteristic spectra and the interatomic spacing. Where (n) is an integer known as the order of reflection, (λ) is the wavelength of the x-rays, (d) is the characteristic spacing between the crystal planes of a given specimen, and (θ) is the angle between the incident beam and the normal to the reflecting lattice plane, as seen in Figure 5.4.[47]

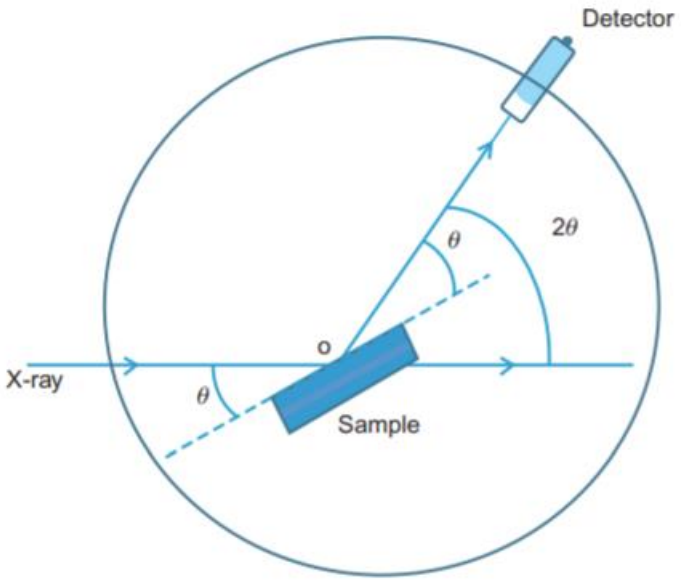

Figure 5.4. X-Ray Diffraction Principle. Adapted from [50] .

By measuring the angles of the x-rays when they reflect on the sample and the interplanar spacings, and comparing this data to the standard line patterns in the Power Diffraction Files (PDF) database, every single crystallographic phase can be determined. It is important to mention that this file is annually updated by the International Center of Diffraction Data (ICDD). [51]

In this thesis, the surface's structure and phase distribution were analyzed by X-ray diffraction (XRD) (X Philips X-Pert) using a Co radiation Kα radiation (λKα1=1.7890Å and λKα2=1.7929Å) at 40kV and 35mA. The experiments were performed in grazing angle geometry of 1° with a step size of 0.025°, and a time per step of 1s, and 2θ range of 20-120°.

5.2. Functional Characterization

The functional characterization was performed in order to evaluate the silver nanoparticles release and its antibacterial activity.

5.2.1. Silver Ion Release

The silver nanoparticles which were deposited onto the nanostructured tantalum oxide substrates are responsible for releasing the silver ions. These silver ions greatly contribute for the antibacterial ability of the samples. Therefore, the silver ion release was studied using the Inductively Coupled Plasma Optical Emission Spectroscopy (ICP-OES) technique.

This process starts with the introduction of a liquid sample into a nebulizer, which transforms it into very small droplets. These droplets are then sprayed into a plasma torch, where the plasma excites the electrons of the sample from the ground state to higher energy levels. Similarly to other techniques, when the electrons fall back into the ground state, they emit wavelength specific photons that are characteristic of a certain element. The intensity of this emission is proportional to the amount of the element present in the sample.

In these experiments, since the nanoporous tantalum samples, which were not submitted to deposition, presented an absence of nanoparticles, they were used as the control samples. While the samples with nanoparticles were used to analyze the silver ions release compared to the control samples.

Firstly, the samples were immersed in a vessel containing 50mL of Phosphate Buffed Saline (PBS) solution. Afterwards, 2mL of this solution were removed from the vessel at different time setpoints: 2h, 24h, 48h, 7d, 14d, 1m. Previous to the analysis, the 2mL of solution were diluted in 4mL of Nitric Acid (HNO_3(2%)), with a dissolution factor of 3 times and then measured by inductively-coupled plasma optical emission spectroscopy (ICP-OES, ICP PerkinElmer spectrometer model Optima 8000).

In order to quantify the silver ion release in an aqueous media, a calibration curve was calculated using a silver Plasma Standard solution (Specpure, 1000 µg/mL). This calibration curve, which is presented in Figure 5.5, was prepared in HNO_3 acid, since that was the matrix in which the silver standard solution was stabilized.

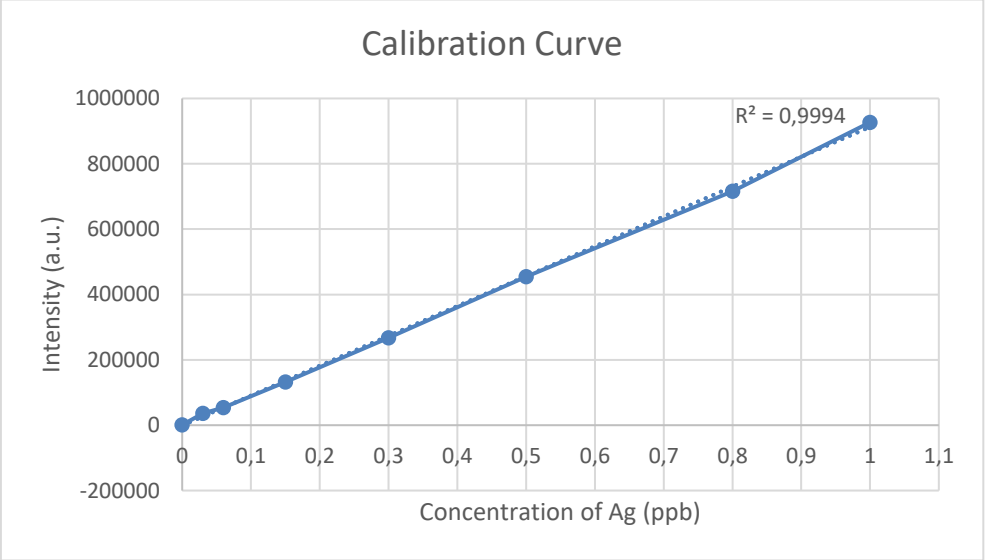

Figure 5.5. ICP-OES Silver calibration curve with Nitric Acid.

5.2.2. Antibacterial Activity

Silver nanoparticles possess three mechanisms capable of causing an antimicrobial effect: (i) release of Ag^+, (ii) generation of free radicals, and (iii) direct contact between the nanoparticles and the bacterial cells. With the purpose of testing the antimicrobial properties of my samples they were subjected to Halo Tests.

The Halos tests were performed by placing the samples in a petri-dish, adding to the plate agar and, lastly, inoculating the bacteria. The samples were introduced in the petri-dish with the coated surface facing down, forcing the contact between the nanoparticles and

the bacteria. The samples were tested against two different bacteria separately: *Staphylococcus Aureus* and *Klebsiella Pneumoniae.*

5.3. Mechanical Characterization

Mechanical characterization techniques were performed to evaluate the coating adhesion to the surface of the samples and the mechanical robustness of each sample.

5.3.1. Adhesion Test

The adhesion test was conducted to evaluate the adhesion of the coating to the substrate. Since the final objective of an implant is to be inserted directly into the bone, it is necessary that the coating stays on the surface while the implant is being screwed, thus maintaining its functionality.

In this thesis, the adhesion test was carried out according to ASTM D3359-17 standards. Each substrate was cut in a checkered pattern, making horizontal and vertical lines with a distance of 1mm between each cut[52]. Then, a specific tape was placed on top of the grided area for 90 seconds and was quickly removed with an angle of 180°.

Following the ASTM D3359-17 standard tests, each sample was analyzed by optical microscopy and rated on a scale from 0B to 5B represented in Figure 5.6.

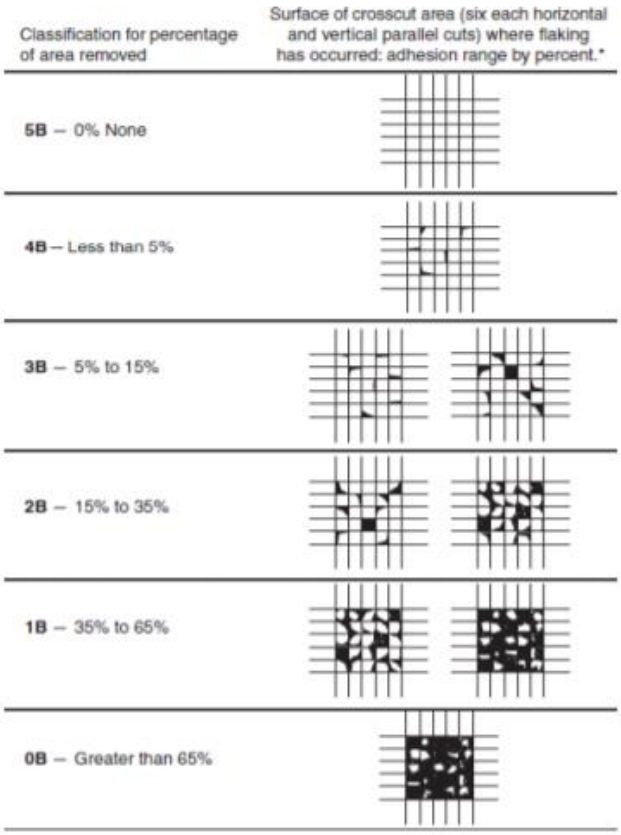

Figure 5.6. Adhesion scale according to ASTM D3359-17, adapted from [52] .

5.3.1. Scratch Test

The mechanical robustness of the samples was evaluated using a scratch tester. During the tests, a progressive load which was setup up to 10N was pressed into each sample by a 1cm viton ball that was adapted to fit the scratch tester, as seen in Figure 5.7. The vertical load rate was set to 100 N/min and the horizontal velocity was programmed to be 30mm/min. Every test was completed using a CSEM Revetest automatic scratch tester.

Following the testing the samples were analyzed by SEM.

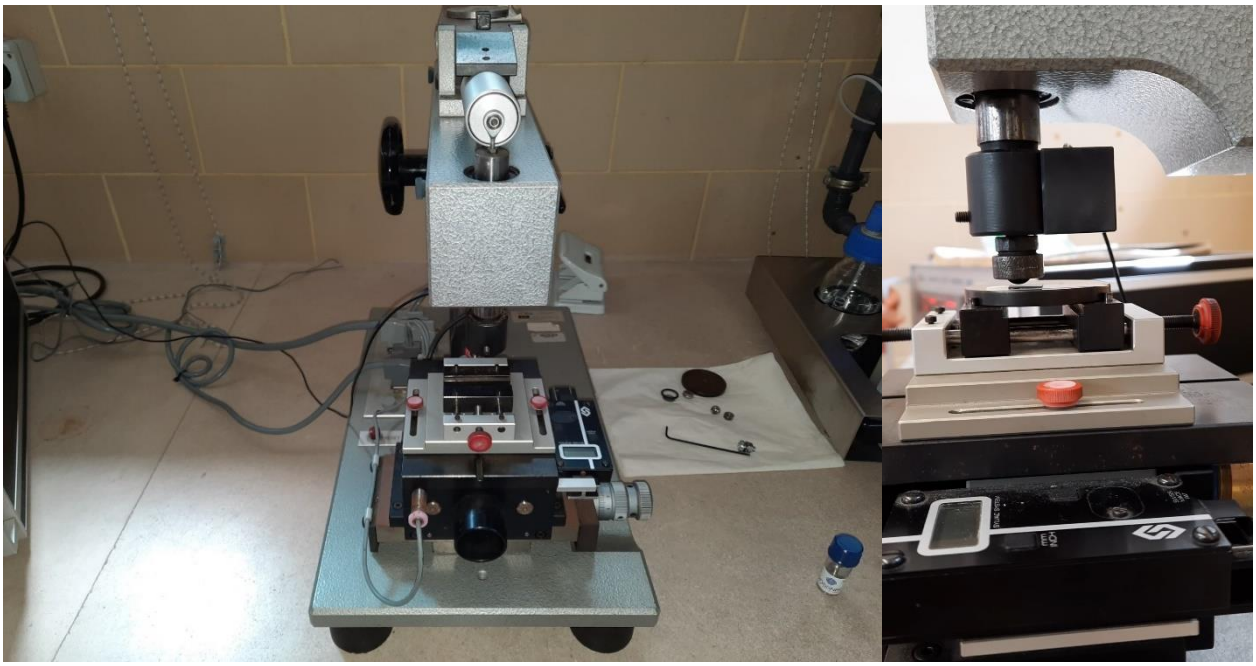

Figure 5.7. Scratch tester adapted with a viton ball.

6. RESULTS AND DISCUSSION

In this chapter, the results obtained from the tests performed on the samples will be presented and analyzed. Furthermore, the impact of the anodization technique and nanoparticle deposition on the physical and chemical properties of the tantalum-based samples will be examined. Additionally, the functional characterization of the surface will be executed, specifically the Ag ion release and the antibacterial activity of each sample. Finally, the mechanical properties of each sample will be analyzed.

6.1. Physical and Chemical Results

6.1.1. Morphology

Figure 6.1. displays the micrographics obtained through SEM, with a scale of 5µm and 1µm, for a standard Ta control sample (Ta), an anodized Ta sample doped with bioactive elements such as Ca and P (Ta_CaP), anodized Ta samples doped with bioactive elements with either 1nm or 2nm silver NPs deposited on its surface (Ta_CaP_1nmAg, Ta_CaP_2nmAg) and anodized Ta samples doped with bioactive elements with 1nm or 2nm Ag NPs deposited on its surface covered by a thin carbon layer (Ta_CaP_1nmAg_C, Ta_CaP_2nmAg_C).

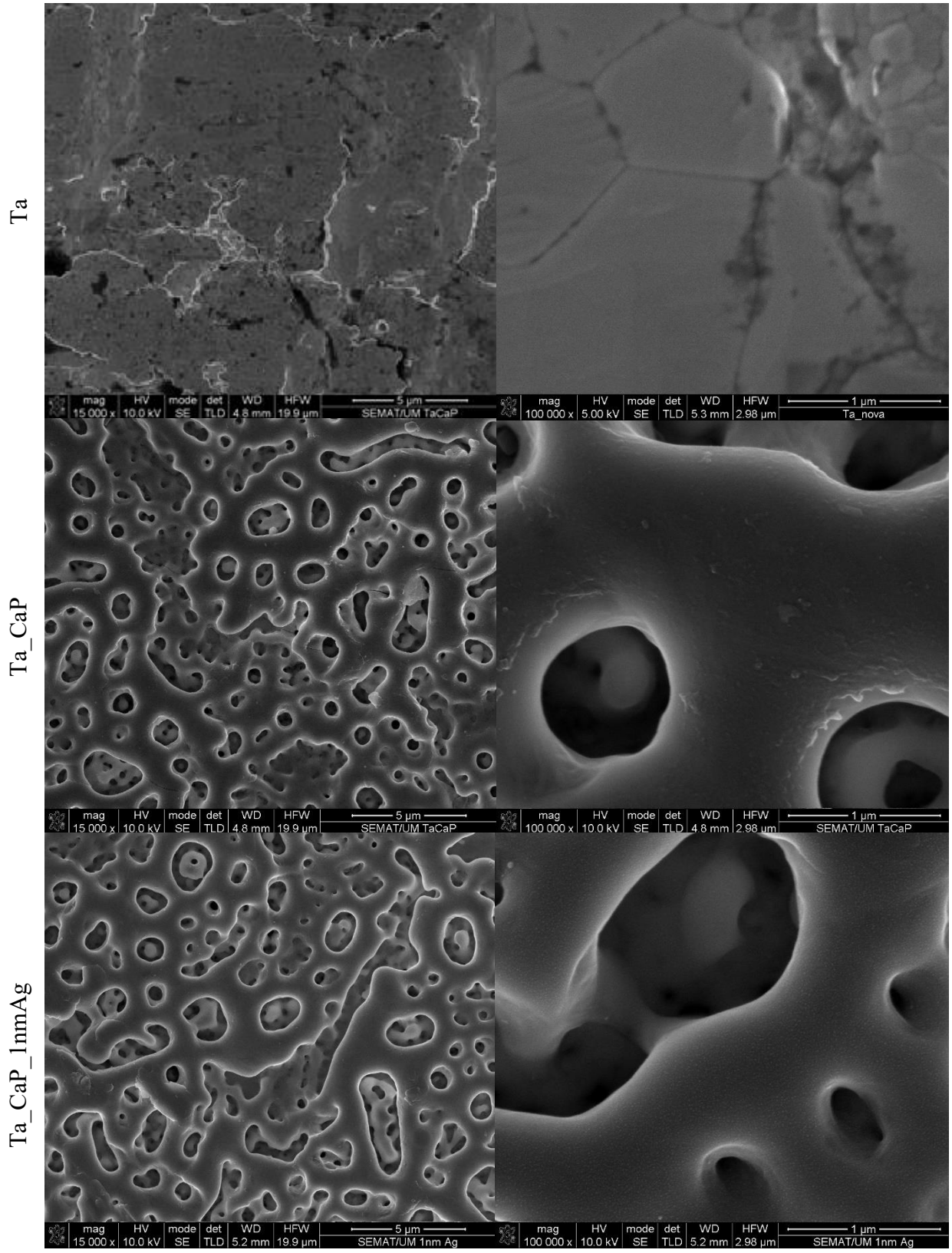
Ta
Ta_CaP
Ta_CaP_1nmAg
mag HV mode det WD HFW 5 µm
15 000 x 10.0 kV SE TLD 4.8 mm 19.9 µm SEMAT/UM TaCaP
mag HV mode det WD HFW 1 µm
100 000 x 5.00 kV SE TLD 5.3 mm 2.98 µm Ta_nova
mag HV mode det WD HFW 5 µm
15 000 x 10.0 kV SE TLD 4.8 mm 19.9 µm SEMAT/UM TaCaP
mag HV mode det WD HFW 1 µm
100 000 x 10.0 kV SE TLD 4.8 mm 2.98 µm SEMAT/UM TaCaP
mag HV mode det WD HFW 5 µm
15 000 x 10.0 kV SE TLD 5.2 mm 19.9 µm SEMAT/UM 1nm Ag
mag HV mode det WD HFW 1 µm
100 000 x 10.0 kV SE TLD 5.2 mm 2.98 µm SEMAT/UM 1nm Ag

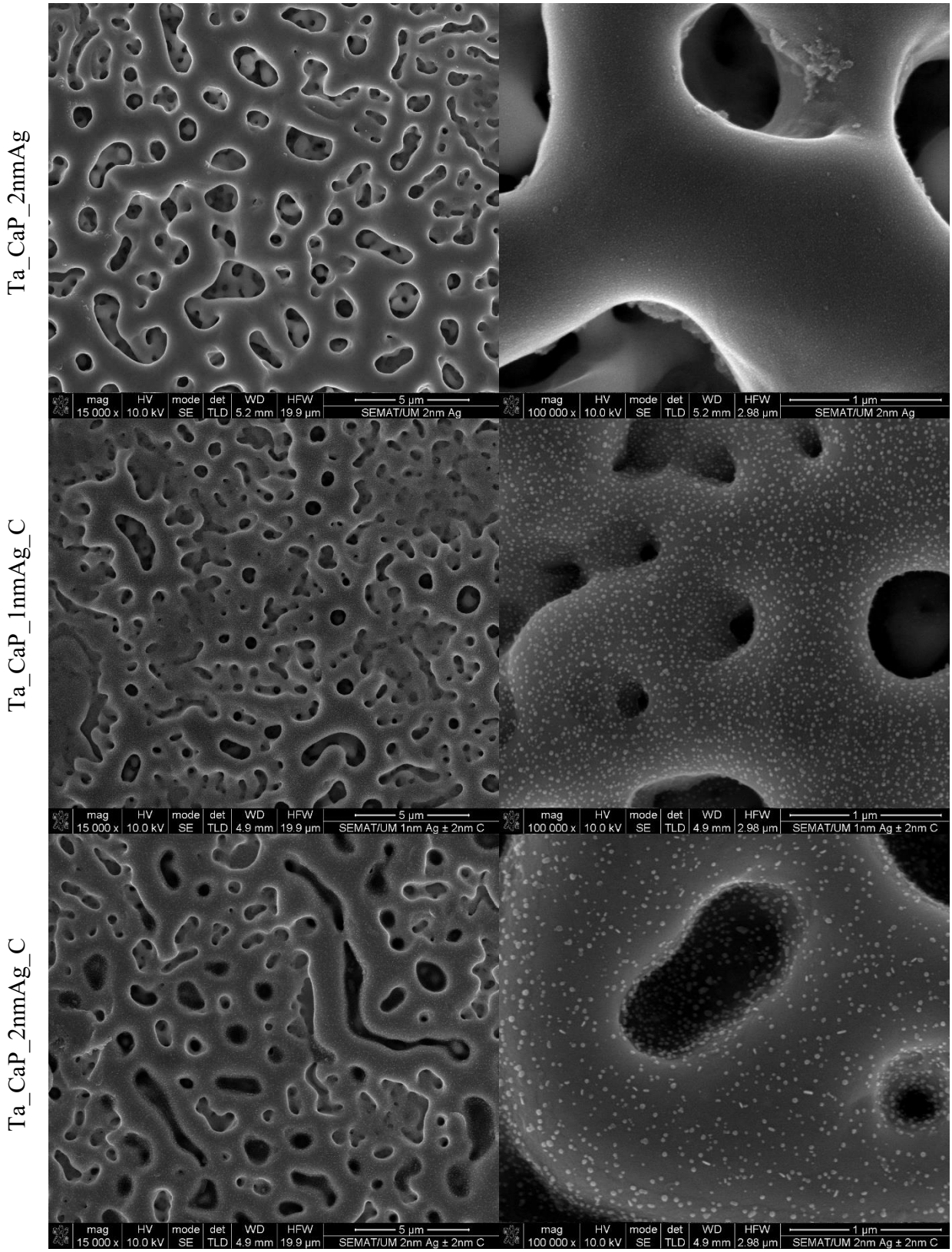

Figure 6.1. SEM micrographics of Ta (Control sample), Ta_CaP, Ta_CaP_1nmAg, Ta_CaP_2nmAg, Ta_CaP_1nmAg_C, Ta_CaP_2nmAg_C. Scales of 5µm and 1µm.

Firstly, by comparing the Ta sample with the Ta_CaP sample, it is possible to verify that the plasma electrolytic oxidation promoted a microstructured surface. Indeed, the Ta_CaP sample successfully mimics the morphology of the bone, since it possesses micro and nanopores, which would promote the osseointegration process.

Secondly, both the Ta_CaP_1nmAg and Ta_CaP_2nmAg samples micrographics confirm the presence of nanoparticles in the form of small spheres. It is important to note that the nanoparticles can be observed, not only on the surface of each sample, but also inside its pores without damaging the bone-like morphology.

Lastly, the couple of micrographics regarding the samples that were covered by a thin carbon layer show the same morphology that resembles the bone, but this time covered by bigger and more spaced nanoparticles, when compared to the Ta_CaP_1nmAg and Ta_CaP_2nmAg micrographics. The change in size and distribution of the nanoparticles can be attributed to the low affinity between the carbon and silver particles. In addition to this factor, silver nanoparticles possess high affinity to each other. Both these characteristics promote the mobility of the silver nanoparticles (maybe occurring during carbon deposition) which aggregate and increase in size.

In order to corroborate this hypothesis further investigation of the SEM micrographics was made using the ImageJ Software. Using this tool, it was possible to differentiate individual from coalesced nanoparticles, as well as calculate the radius of each nanoparticle. All this data is depicted in Figure 6.2.

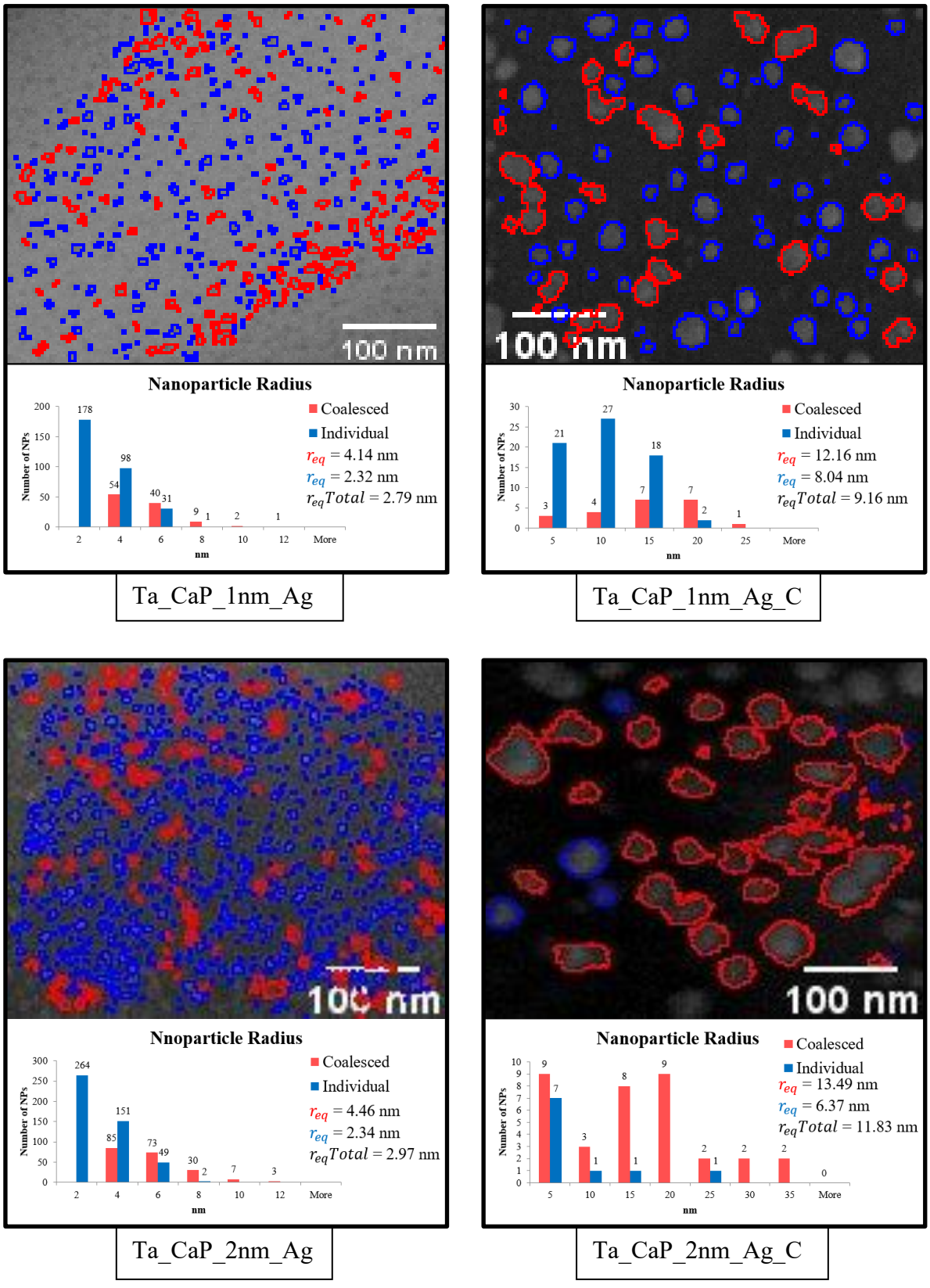

Figure 6.2. Differentiation between Coalesced and Individual nanoparticles. Graph representing the number and size of the nanoparticles present in each sample.

6.1.2. Topography

The topographical characterization of the samples was performed by AFM. Figure 6.3 displays the topography of the pure Ta standard sample and the Ta_CaP sample, with a scale of 10µm. Through the observation of this Figure it is possible to identify pores created by the PEO technique, further confirming that the Ta_CaP's surface mimics the bone structure.

The AFM technique, allied with the usage of the Gwyddion Software made it possible to calculate both the area mean roughness (Sa) and the area quadratic roughness (Sq) of each sample. As represented in Table 6.1, the roughness of the Ta_CaP sample is higher than the roughness of the standard Ta sample, due to the porosity that the Ta_CaP sample obtained through PEO treatment.

Figure 6.4. shows the AFM results of the: Ta_CaP,Ta_CaP_1nmAg, Ta_CaP_2nmAg, Ta_CaP_1nmAg_C and Ta_CaP_2nmAg_C samples, with a scale of 0.5µm. A careful examination of the Ta_CaP sample image confirms the absence of nanoparticles, contrasting with all the other images of the samples present in Figure 6.4, where it is possible to identify the presence of nanoparticles in the form of small spheres. As expected, the deposition of nanoparticles on the surface of the sample increased its roughness, as seen in Table 6.1.

Furthermore, the images from Figure 6.4 of the Ta_CaP_1nmAg_C and Ta_CaP_2nmAg_C confirm the presence of bigger and more spaced nanoparticles when compared to their carbon-less counterparts. Finally, Table 6.1 shows a small decrease in roughness with the addition of the thin carbon layer, since it covers some of the pores.

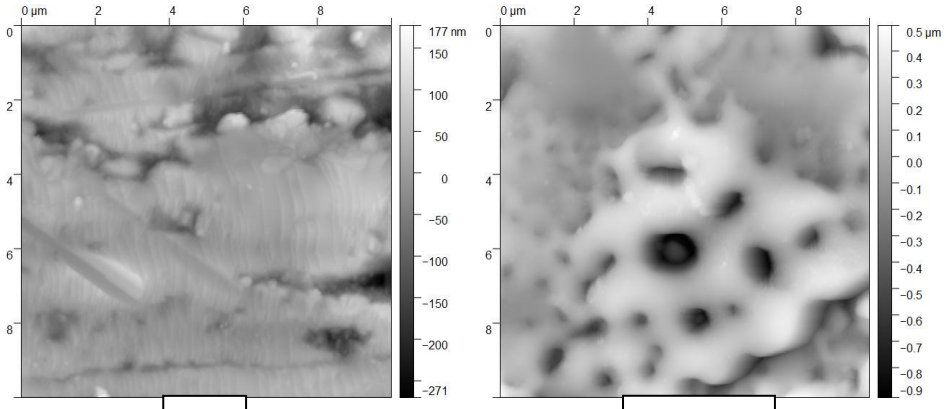

Figure 6.3. AFM image of the Ta and Ta_CaP samples. Scale of 10µm.

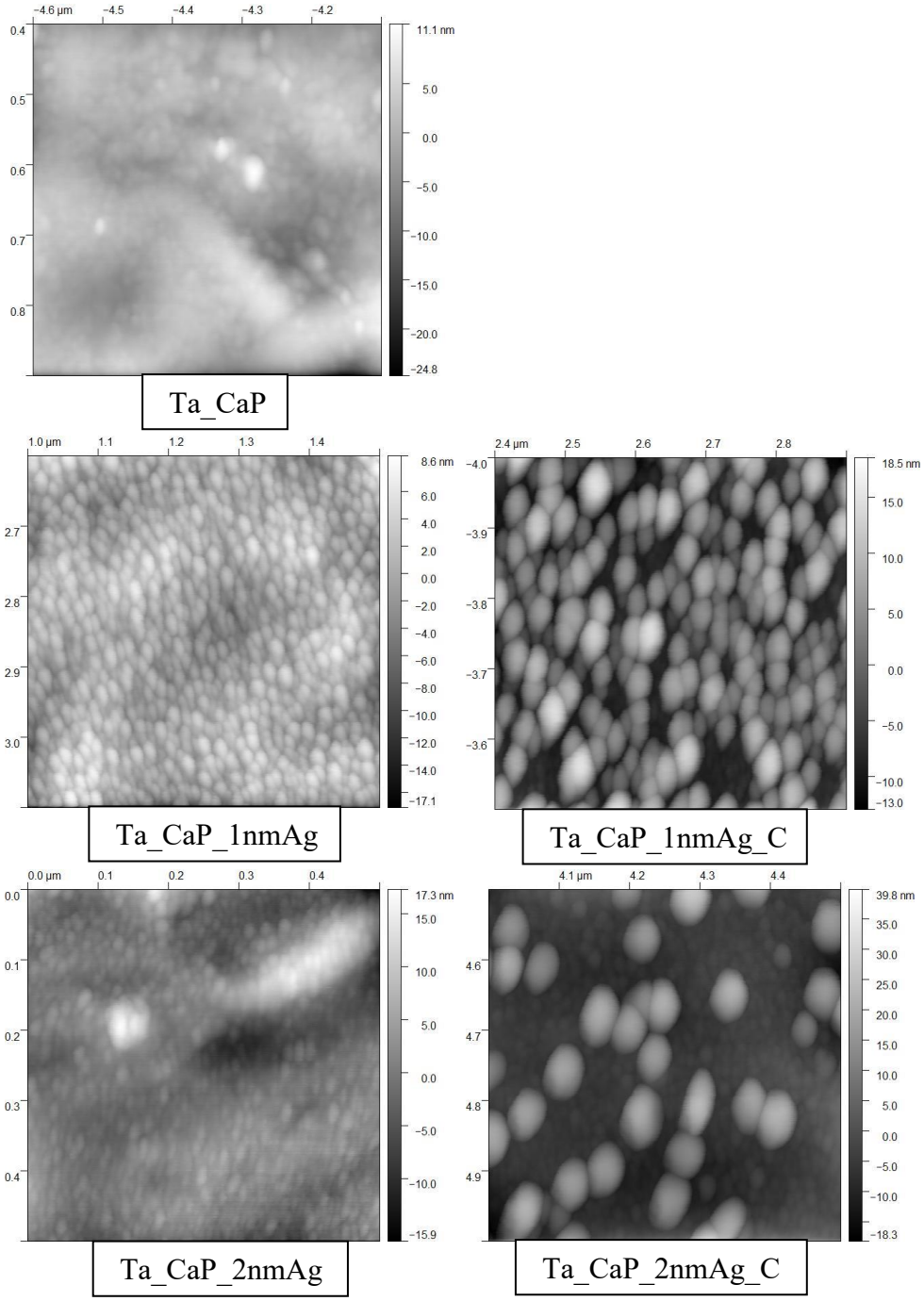

Figure 6.4. AFM images of the: Ta_CaP, Ta_CaP_1nmAg, Ta_CaP_2nmAg, Ta_CaP_1nmAg_C and Ta_CaP_2nmAg_C samples. Scale of 0.5µm.

Sample	Area Mean Roughness (Sa) (nm)	Area Square Roughness (Sq) (nm)
Ta	32	45
Ta_CaP	151	200
Ta_CaP_1nmAg	183	234
Ta_CaP_1nmAg_C	149	190
Ta_CaP_2nm	228	283
Ta_CaP_2nmAg_C	174	220

Table 6.1. Area Mean Roughness and Area Square Roughness of the: Ta, Ta_CaP, Ta_CaP_1nmAg, Ta_CaP_2nmAg, Ta_CaP_1nmAg_C and Ta_CaP_2nmAg_C samples.

6.1.3. Chemical Composition

The chemical composition analysis was performed by SEM-EDS. This technique granted information about the atomic percentage of each chemical element present in several locations of each sample. Table 6.2 presents the average results regarding the atomic percentage of the chemical elements. The information drawn from the Table made it possible to reach various critical conclusions.

First of all, the PEO technique was able to simultaneously create a porous oxide layer and incorporate bioactive elements (Ca, P). The information from Table 6.2 regarding the Ta_CaP sample further supports the conclusion that it mimics the bone, since it not only possesses similar morphology (from previous SEM images), but also has in its composition the same bioactive elements. It is important to notice that the Ca/P ratio from this sample is 3, which is a higher value than the one optimal for the creation of crystalline hydroxyapatite (1.67).

Regarding Ta_CaP_1nmAg sample's information in Table 6.2, it made it possible to verify the presence of the silver element. Furthermore, the atomic percentage of the silver element nearly doubled in the Ta_CaP_2nmAg sample. This is according to expectations since its deposition time was also two times greater.

Finally, both Ta_CaP_1nmAg_C and Ta_CaP_2nmAg_C samples display similar silver atomic percentage values when compared to their carbon-less counterparts (≈1 at.% and ≈2 at.%, respectively). The chemical composition analysis of these samples also confirmed the presence of the carbon element in similar atomic percentages on both.

Sample	Ta (at.%)	O (at.%)	Ca (at.%)	P (at.%)	Ag (at.%)	C (at.%)
Ta	≈100	-	-	-	-	-
Ta_CaP	84	12	3	1	-	-
Ta_CaP_1nmAg	83	12	3	1	1	-
Ta_CaP_1nmAg_C	82	12	3	1	1	1
Ta_CaP_2nmAg	81	12	4	1	2	-
Ta_CaP_2nmAg_C	80	12	4	1	2	1

Table 6.2. Atomic percentage of the chemical elements present in the: Ta, Ta_CaP, Ta_CaP_1nmAg, Ta_CaP_2nmAg, Ta_CaP_1nmAg_C and Ta_CaP_2nmAg_C samples.

6.1.4. Crystalline Structure

The XRD results for the crystalline structures present in the samples are displayed as a diffractogram in Figure 6.5.

Comparing the spectra for the samples with the Power Diffraction Files from ICDD it is possible to verify that the only crystalline structure present in the samples is the α-Ta phase (ICDD nº 00-004-0788), from the substrate Ta sheet.

None of the samples subjected to the PEO treatment possess peaks in their spectra corresponding to a crystalline phase of tantalum oxide (Ta_2O_5), which was previously proven to be present on the surface of the samples. This fact can be justified, since the temperatures needed to obtain the crystalline form of Ta_2O_5 are higher than the ones achieved by PEO, which means that the tantalum oxide is present in the samples under its amorphous phase. Additionally, the absence of calcium phosphate in the spectra can also be justified by the same reason.

The lack of silver and carbon peaks on the spectrums of the samples that possess these elements can be attributed to the superficiality, as well as its very low amount of these particles, which means that they cannot be detected by XRD.

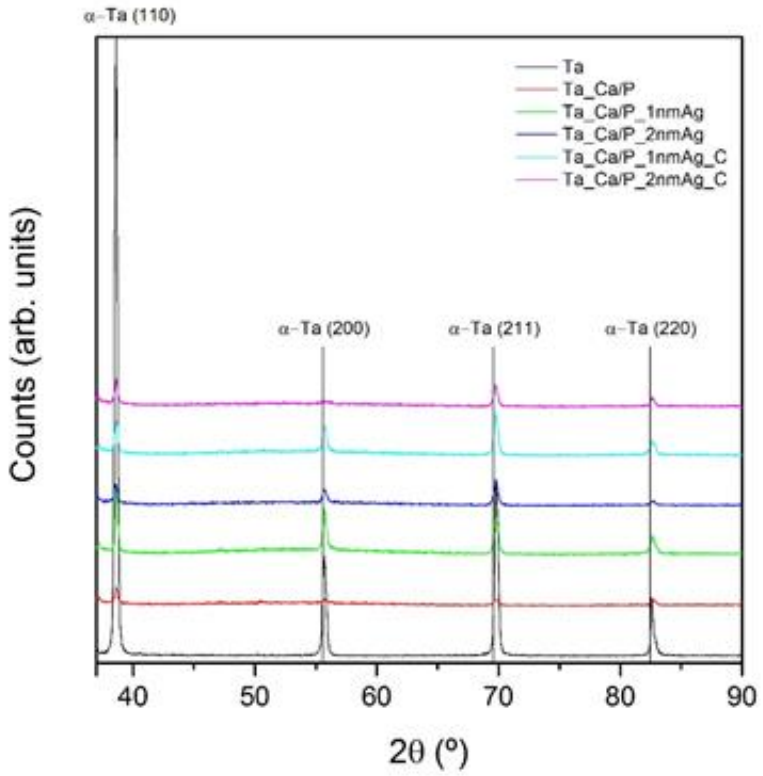

Figure 6.5. Crystalline structures diffractogram of the: Ta, Ta_CaP, Ta_CaP_1nmAg, Ta_CaP_2nmAg, Ta_CaP_1nmAg_C and Ta_CaP_2nmAg_C samples.

6.2. Functional Results

6.2.1. Silver Ion Release

The ICP-OES results regarding the silver ion release of the samples are depicted in Figure 6.6. This graph contradicts the expectations that the thin carbon layer would control the Ag^+ release. Instead, the Ta_CaP_1nmAg_C and Ta_CaP_2nm_C samples showed higher ionization rates in relation to the carbon-less coatings. Figure 6.6 also reveals that the samples containing carbon have not yet stabilized and continue to release silver ions throughout the whole month. Oppositely the carbon-less samples have stabilized. This can be stated since the release line of the samples that do not possess carbon have turned horizontal with the passing of time.

In order to confirm this information, the samples were submitted to SEM analysis. Figure 6.7 shows a comparison before and after of the ICP-OES testing. This comparison shows that silver nanoparticles can still be seen in Ta_CaP_1nmAg_C and Ta_CaP_2nmAg_C samples, confirming that there is still silver on the surface of the

substrates to be ionized. Contrarily, the images regarding the Ta_CaP_1nmAg and Ta_CaP_2nmAg samples show that the silver nanoparticles that were present on the surface have almost all been released. Therefore, the information depicted from the graph is coherent with the SEM images.

According to Manninen *et al* [53] coatings that possess silver and carbon show higher ionization rates since they form nano-galvanic couples. Therefore, such material configuration promotes galvanic corrosion of the phase with lower reduction potential, in this case: silver.

Nevertheless, even with this enhancement of the ionization of the biocidal Ag^{+}, the cumulative values show very minimal silver release from the samples. This fact means that the quantity of silver deposited onto the substrates was not sufficient and will not present antibacterial activity.

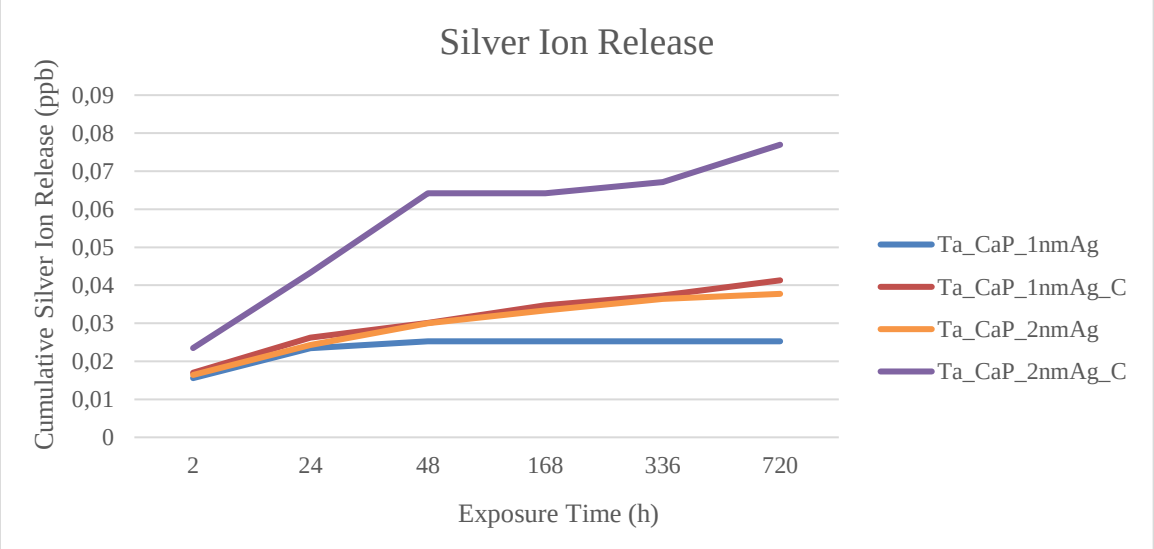

Figure 6.6. ICP-OES results of the silver Ion Release of the: Ta_CaP_1nmAg, Ta_CaP_2nmAg, Ta_CaP_1nmAg_C and Ta_CaP_2nmAg_C samples.

Before ICP-OES

After ICP-OES

Ta CaP 1nmAg

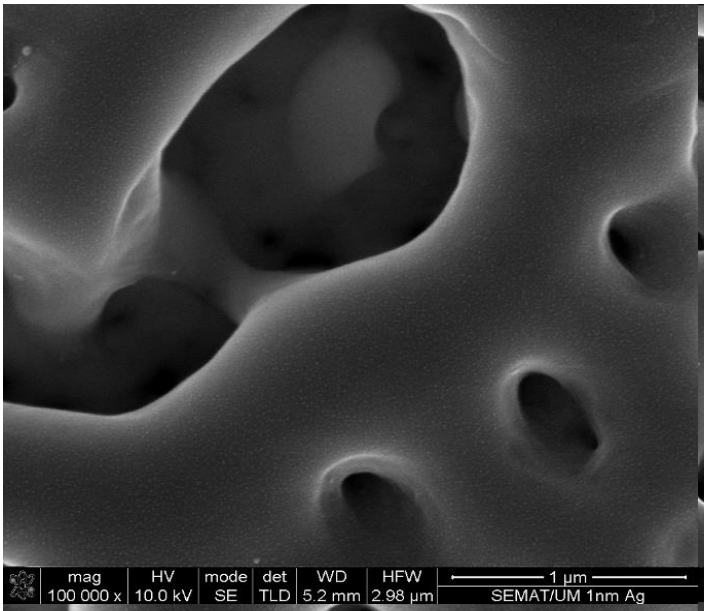

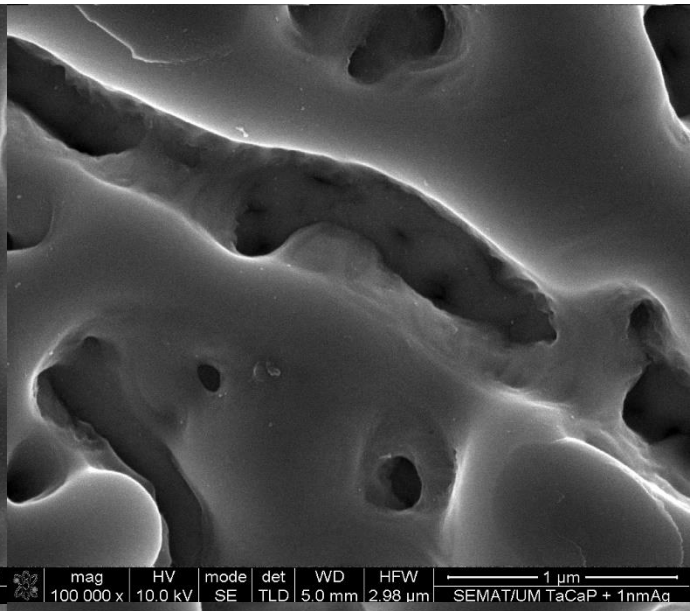

Ta CaP 2nmAg

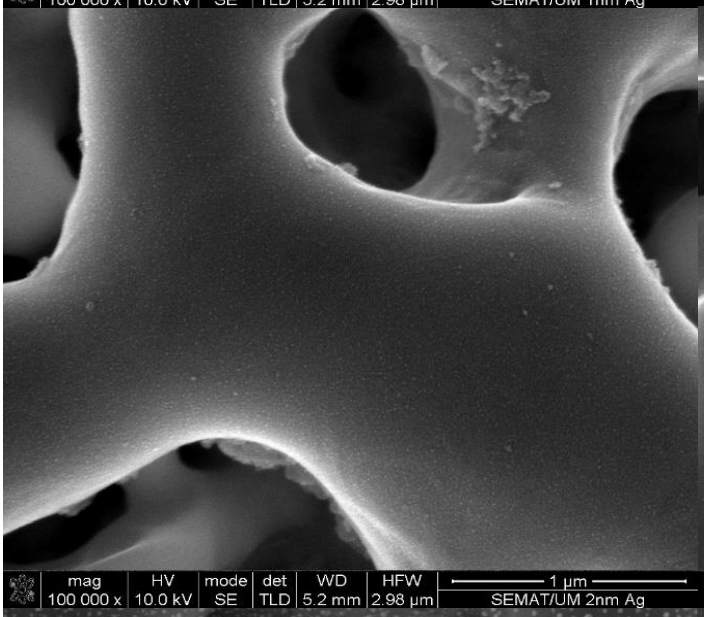

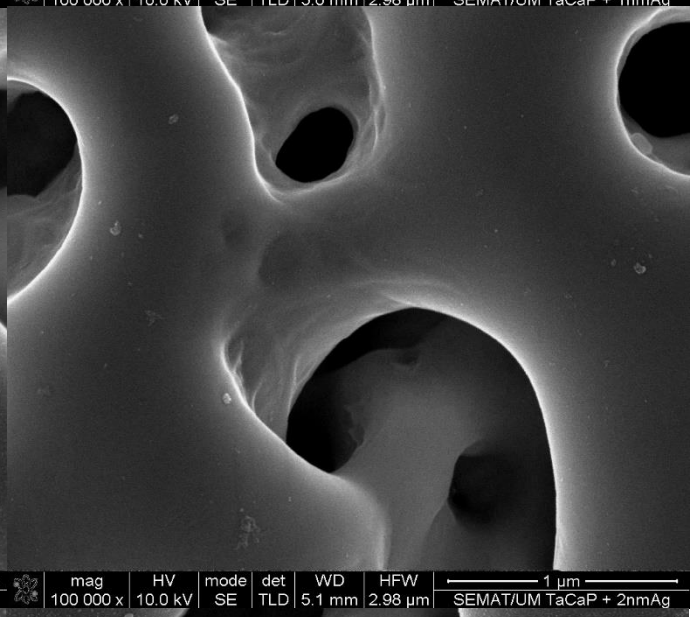

Ta_CaP_1nmAg_C

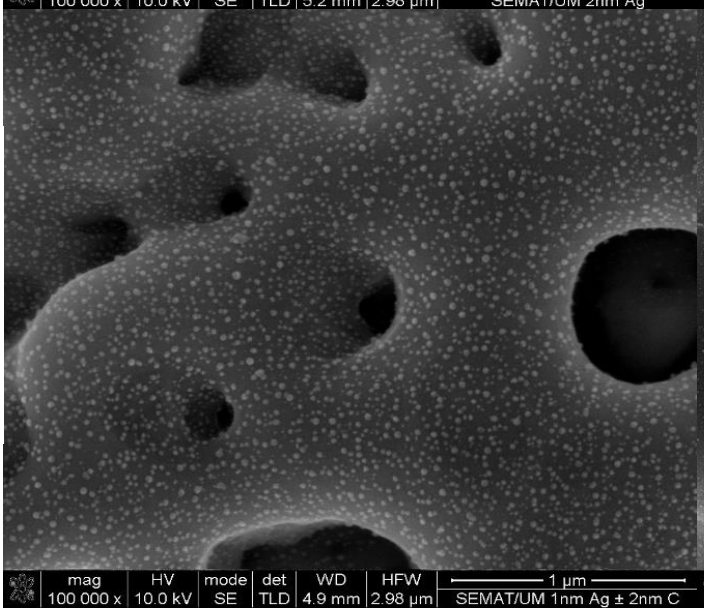

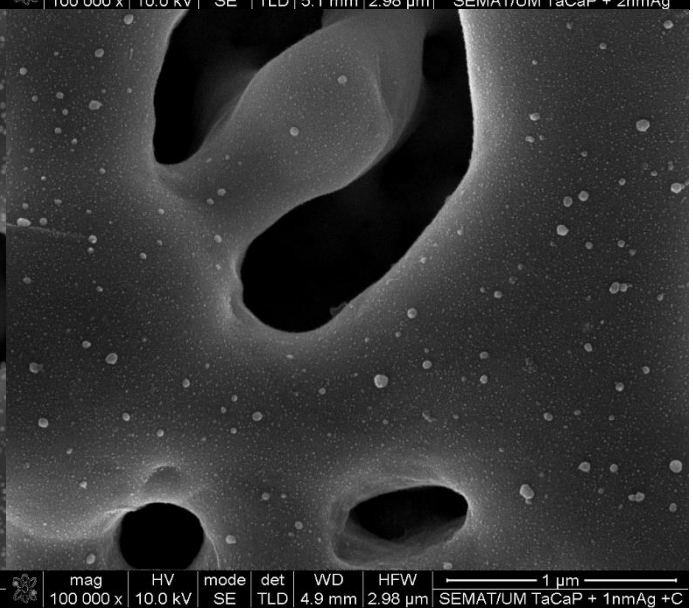

Ta_CaP_2nmAg_C

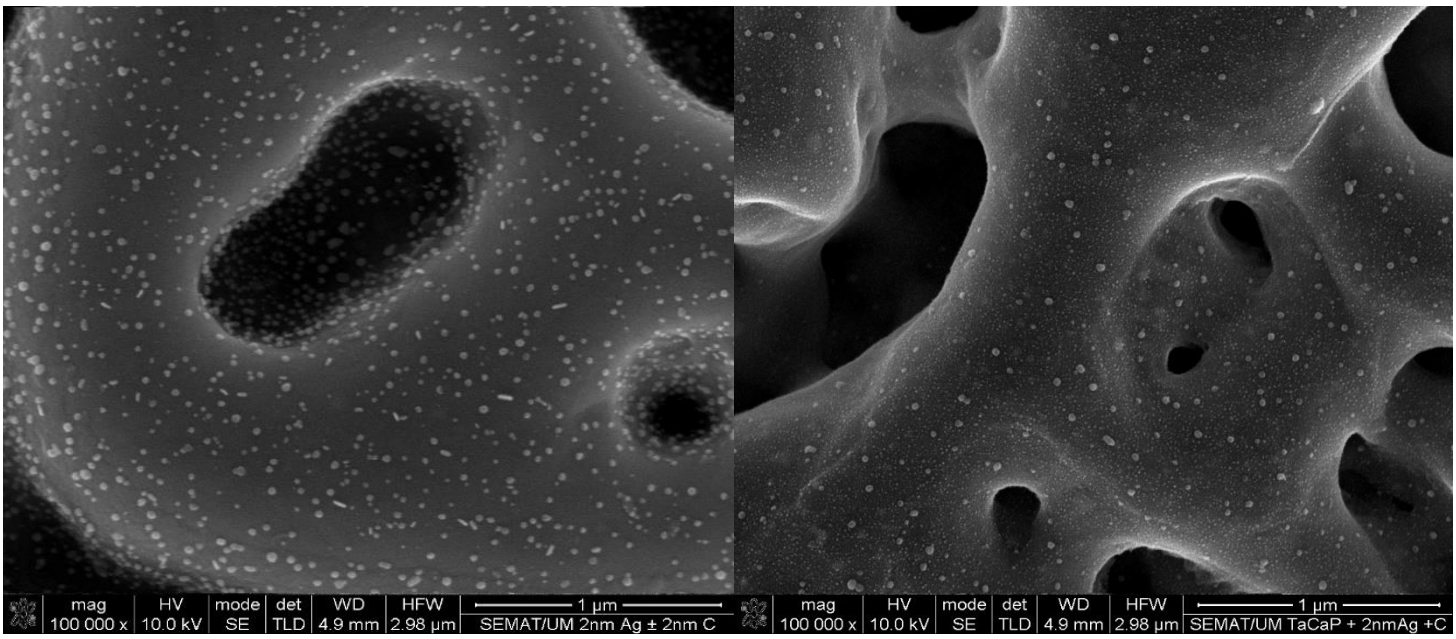

Figure 6.7. SEM images comparing the before and after of the ICP-OES test of the: Ta_CaP_1nmAg, Ta_CaP_2nmAg, Ta_CaP_1nmAg_C and Ta_CaP_2nmAg_C samples.

6.2.1. Antibacterial Activity

The results from the Halo tests confirmed that the samples possess no antibacterial activity. Figure 6.8 shows the end result of the test for both *Staphylococcus Aureus* and *Klebsiella Pneumoniae*, where it cannot be seen any halo inhibition zone.

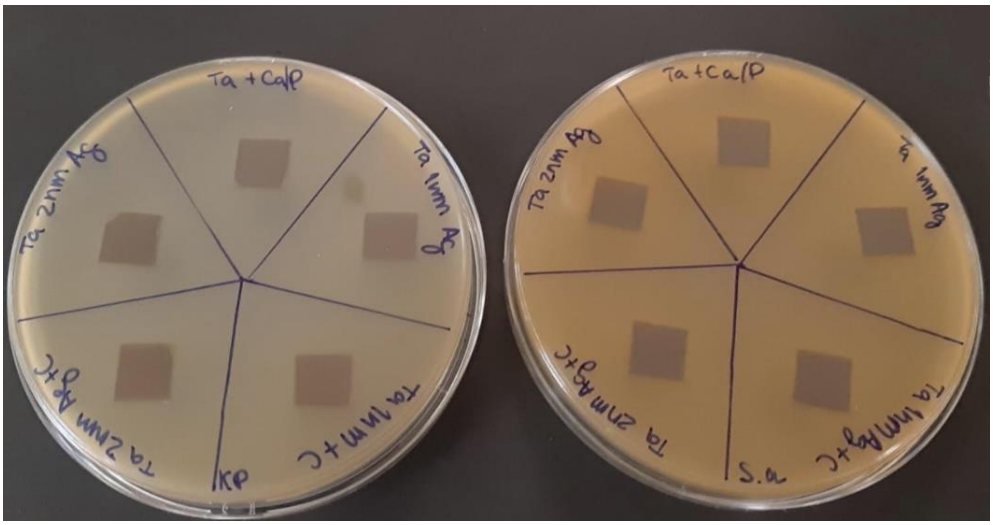

Figure 6.8. Halo test results of the: Ta_CaP, Ta_CaP_1nmAg, Ta_CaP_2nmAg, Ta_CaP_1nmAg_C and Ta_CaP_2nmAg_C samples.

6.3. Mechanical Results

6.3.1. Adhesion Test

The results from the adhesion tests show very positive results, since there was a complete adhesion of the coating to each sample. Optical microscopy images, such as Figure 6.9, show that apart from the cuts made to the sample there was no removal of the coating by the specific tape, according to the ASTM 03359-17 standard adhesion test.

Therefore, according to Figure 5.6, the samples were classified as 5B, since there was no area removed.

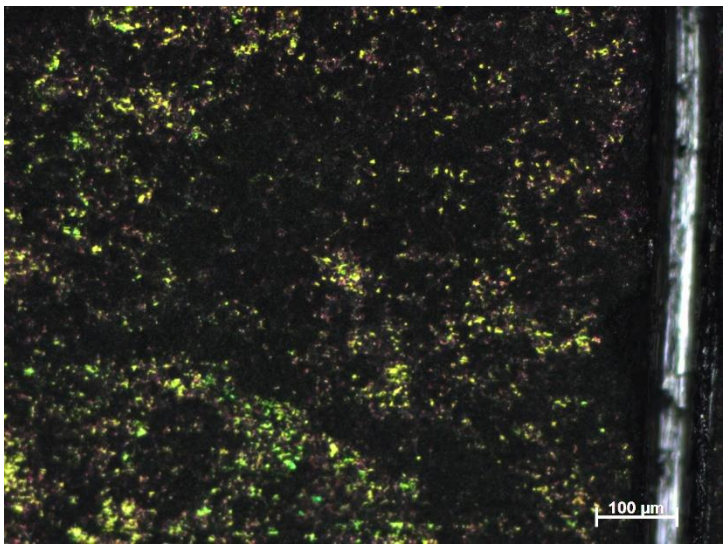

Figure 6.9. 10x optical microscopy of the Ta_CaP_2nmAg sample.

6.3.2. Scratch Test

The scratch test results show that the carbon layer might have the promising ability of improving the mechanical robustness of the samples and even in some cases prevent the removal of the silver nanoparticles. Figure 6.10 shows a comparison of the before and after scratch test.

The first sample to be tested was Ta_CaP_1nmAg. SEM results show that this coating was completely crushed by the scratch test, destroying the micro and nanopores that previously existed on the surface. Additionally, it is important to mention that the nanoparticles were completely removed from the surface.

Afterwards, the Ta_CaP_1nmAg_C sample was submitted to the scratch test and analyzed. The SEM images regarding this sample show micro and nanopores still present on

the sample. Even though the coating maintained its porosity, it is possible to see that it is partially shattered. The shattering of the coating can be perceived as a positive feature of the sample, as it can prevent damage to the bone. From this Figure it is also important to notice that the carbon layer did not prevent totally the removal of the silver nanoparticles.

The test to the Ta_CaP_2nmAg sample was performed next. This coating showed very similar behavior to the Ta_CaP_1nmAg sample's coating, since it could not withstand the scratch test and was completely crushed by it.

Finally, the Ta_CaP_2nmAg_C sample was submitted to the test. This coating displayed the best results when compared to the other samples, since it, not only, maintained its porosity while partially shattered, but also prevented the silver nanoparticles to be totally removed from the surface. These results can be related somehow with tribological behavior attributed to the carbon layer, recognized with low friction coefficient.

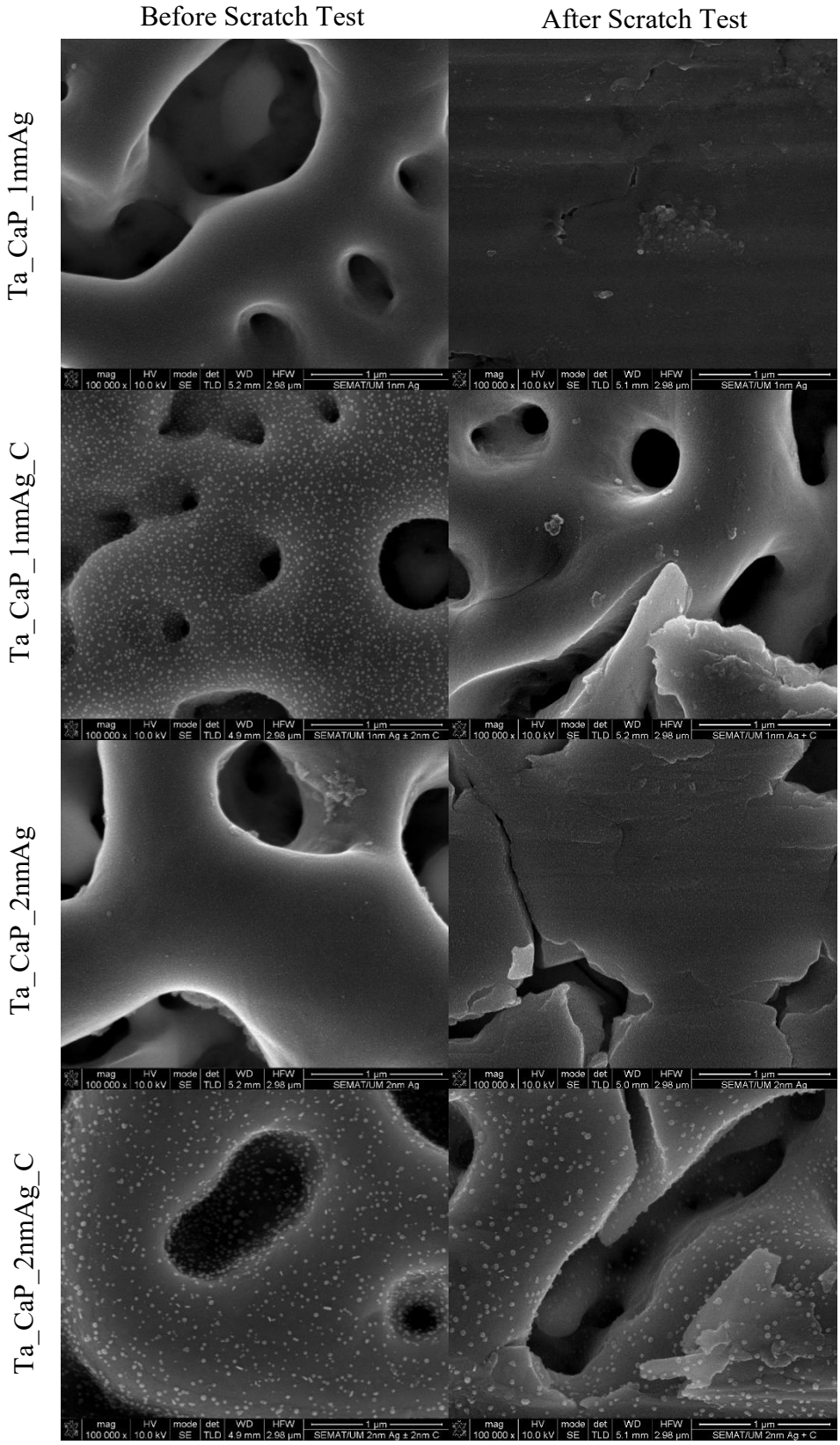

Figure 6.10. Before and after scratch test of the Ta_CaP_1nmAg, Ta_CaP_1nmAg_C, Ta_CaP_2nmAg and Ta_CaP_2nmAg_C samples.

7. CONCLUSIONS AND FUTURE WORK

Different sized silver nanoparticles were sputtered onto tantalum oxide with micro and nanopores. These samples were produced in order to achieve nanostructured samples with antibacterial activity suitable for a biomaterial. The porous tantalum oxide nanostructures were created by performing PEO to high-purity tantalum sheets. Afterwards, silver nanoparticles with 1nm and 2nm were deposited onto the manufactured substrates through magnetron sputtering. Then, some of these samples were covered by a thin carbon layer, using the same method. The samples were then submitted to characterization techniques in order to evaluate their physical, chemical, functional and mechanical properties.

Morphologically, every sample presented micro and nanopores which means the PEO technique was successful. It is also possible to observe silver nanoparticles on the surface of the sputtered substrates. The topography results confirmed the fact that the PEO technique created porosity since the mean roughness of the treated samples is higher than the pure Ta sheets. The chemical composition of the samples reported an incorporation of bioactive elements such as Ca and P during the PEO treatment. Furthermore, it confirmed the presence of silver and carbon on the substrates when they were deposited.

The ICP-OES results regarding the silver ion release showed that the samples that were covered with carbon exhibited higher ionization rates since silver and carbon form a nano-galvanic couple which promotes the galvanic corrosion of silver. However, even with the higher ionization rates, the ICP-OES cumulative results of ionization show very minimal silver release, which means that the quantity of silver NPs sputtered onto the substrate was not sufficient to produce antibacterial activity. Halo tests confirmed the suspicion that there was no antibacterial activity on the samples.

Mechanical characterization techniques revealed that the coating showed good adhesion to the surface. Additionally, it appears that the carbon layer has the ability of improving the mechanical robustness of the samples and in some cases preventing the removal of nanoparticles. However, it is important to mention that the robustness of the samples is a parameter that requires further investigation in order to achieve a dental implant with the mechanical robustness to withstand surgery procedure.

In future works, the deposition of more/bigger silver nanoparticles, while avoiding the formation of a film layer, can be an interesting starting point.

Furthermore, in order to create a functioning prototype, it will be crucial to test several carbon layers with different thicknesses to increase the mechanical robustness while further promoting the release of silver ions through nano-galvanic corrosion.

BIBLIOGRAPHY

1. Hildebrand C, Fried K, Tuisku F, Johansson CS. Teeth and tooth nerves. *Prog Neurobiol*. 1995;45(3):165-222. doi:10.1016/0301-0082(94)00045-J
2. Agulyansky A. INTRODUCTION. In: *Chemistry of Tantalum and Niobium Fluoride Compounds*. Elsevier; 2004:1-10. doi:10.1016/b978-044451604-6/50001-x
3. Yang Z, Xi Y, Bai J, et al. Covalent grafting of hyperbranched poly-L-lysine on Ti-based implants achieves dual functions of antibacteria and promoted osteointegration in vivo. *Biomaterials*. 2021;269:120534. doi:10.1016/j.biomaterials.2020.120534
4. Zafar MS, Najeeb S, Khurshid Z. Introduction to dental implants materials, coatings, and surface modifications. In: *Dental Implants*. Elsevier; 2020:1-4. doi:10.1016/b978-0-12-819586-4.00001-9
5. Guo T, Gulati K, Arora H, Han P, Fournier B, Ivanovski S. Race to invade: Understanding soft tissue integration at the transmucosal region of titanium dental implants. *Dent Mater*. Published online March 4, 2021. doi:10.1016/j.dental.2021.02.005
6. Sakka S, Baroudi K, Nassani MZ. Factors associated with early and late failure of dental implants. *J Investig Clin Dent*. 2012;3(4):258-261. doi:10.1111/j.2041-1626.2012.00162.x
7. Tanner A, Maiden MFJ, Lee K, Shulman LB, Weber HP. Dental Implant Infections. *Clin Infect Dis*. 1997;25(s2):S213-S217. doi:10.1086/516243
8. Liaw K, Delfini RH, Abrahams JJ. Dental Implant Complications. *Semin Ultrasound, CT MRI*. 2015;36(5):427-433. doi:https://doi.org/10.1053/j.sult.2015.09.007
9. Zhao Y, Pu R, Qian Y, Shi J, Si M. Antimicrobial photodynamic therapy versus antibiotics as an adjunct in the treatment of periodontitis and peri-implantitis: A systematic review and meta-analysis. *Photodiagnosis Photodyn Ther*. 2021;34:102231. doi:10.1016/j.pdpdt.2021.102231
10. Song X, Li L, Gou H, Xu Y. Impact of implant location on the prevalence of peri-implantitis: A systematic review and meta- analysis. *J Dent*. 2020;103:103490.

doi:10.1016/j.jdent.2020.103490

11. Kotsailidi EA, Michelogiannakis D, Al-Zawawi AS, Javed F. Surgical or non-surgical treatment of peri-implantitis — what is the verdict?,. *Surg Pract Sci*. 2020;1:100010. doi:10.1016/j.sipas.2020.100010
12. Oliveira J. Deposition of Zn-ZnO nanoparticles by magnetron sputtering onto tantalum substrates. Published online 2017.
13. Wirth J, Tahriri M, Khoshroo K, Rasoulianboroujeni M, Dentino A, Tayebi L. Surface modification of dental implants. In: *Biomaterials for Oral and Dental Tissue Engineering*. ; 2017:85-96. doi:10.1016/B978-0-08-100961-1.00006-2
14. Krishnakumar S, Senthilvelan T. Polymer composites in dentistry and orthopedic applications-a review. *Mater Today Proc*. Published online October 2, 2020. doi:10.1016/j.matpr.2020.08.463
15. Perrotti V, Iaculli F, Fontana A, Piattelli A, Iezzi G. Introduction to bone response to dental implant materials. In: *Bone Response to Dental Implant Materials*. Elsevier Inc.; 2017:1-23. doi:10.1016/B978-0-08-100287-2.00001-X
16. Lemons JE, Misch-Dietsh F, McCracken MS. Biomaterials for Dental Implants. In: *Dental Implant Prosthetics*. Elsevier Inc.; 2015:66-94. doi:10.1016/B978-0-323-07845-0.00004-X
17. Chen CS, Chang JH, Srimaneepong V, et al. Improving the in vitro cell differentiation and in vivo osseointegration of titanium dental implant through oxygen plasma immersion ion implantation treatment. *Surf Coatings Technol*. 2020;399:126125. doi:10.1016/j.surfcoat.2020.126125
18. Fialho L, Grenho L, Fernandes MH, Carvalho S. Porous tantalum oxide with osteoconductive elements and antibacterial core-shell nanoparticles: A new generation of materials for dental implants. *Mater Sci Eng C*. 2021;120:111761. doi:10.1016/j.msec.2020.111761
19. Kommel L, Shahreza BO, Mikli V. Microstructure and physical-mechanical properties evolution of pure tantalum processed with hard cyclic viscoplastic deformation. *Int J Refract Met Hard Mater*. 2019;83:104983. doi:10.1016/j.ijrmhm.2019.104983
20. Black J. Biologic performance of tantalum. *Clin Mater*. 1994;16(3):167-173. doi:10.1016/0267-6605(94)90113-9

21. MOSHIER RW. INTRODUCTION. In: *Analytical Chemistry of Niobium and Tantalum*. Elsevier; 1964:1-10. doi:10.1016/b978-0-08-010418-8.50004-7
22. Niu Y, Chen M, Wang J, et al. Preparation and thermal shock performance of thick α-Ta coatings by direct current magnetron sputtering (DCMS). *Surf Coatings Technol*. 2017;321:19-25. doi:10.1016/j.surfcoat.2017.04.045
23. Garg SP, Krishnamurthy N, Awasthi A, Venkatraman M. The O-Ta (Oxygen-Tantalum) system. *J Phase Equilibria*. 1996;17(1):63-77. doi:10.1007/BF02648373
24. Almeida Alves CF, Calderon VS, Ferreira PJ, Marques L, Carvalho S. Passivation and dissolution mechanisms in ordered anodic tantalum oxide nanostructures. *Appl Surf Sci*. 2020;513:145575. doi:10.1016/j.apsusc.2020.145575
25. Huang HL, Tsai MT, Lin YJ, Chang YY. Antibacterial and biological characteristics of tantalum oxide coated titanium pretreated by plasma electrolytic oxidation. *Thin Solid Films*. 2019;688:137268. doi:10.1016/j.tsf.2019.04.043
26. Anil S, Venkatesan J, Shim MS, Chalisserry EP, Kim SK. Bone response to calcium phosphate coatings for dental implants. In: *Bone Response to Dental Implant Materials*. Elsevier Inc.; 2017:65-88. doi:10.1016/B978-0-08-100287-2.00004-5
27. Njuguna J, Ansari F, Sachse S, Zhu H, Rodriguez VM. Nanomaterials, nanofillers, and nanocomposites: Types and properties. In: *Health and Environmental Safety of Nanomaterials: Polymer Nancomposites and Other Materials Containing Nanoparticles*. Elsevier Ltd.; 2014:3-27. doi:10.1533/9780857096678.1.3
28. Leon L, Chung EJ, Rinaldi C. A brief history of nanotechnology and introduction to nanoparticles for biomedical applications. In: *Nanoparticles for Biomedical Applications: Fundamental Concepts, Biological Interactions and Clinical Applications*. Elsevier; 2019:1-4. doi:10.1016/B978-0-12-816662-8.00001-1
29. Paris JL, Vallet-Regí M. Nanostructures for imaging, medical diagnostics and therapy. In: *Fundamentals of Nanoparticles: Classifications, Synthesis Methods, Properties and Characterization*. Elsevier; 2018:1-28. doi:10.1016/B978-0-323-51255-8.00001-X
30. Martínez R, Navarro Poupard MF, Álvarez A, et al. Nanoparticle behavior and stability in biological environments. In: *Nanoparticles for Biomedical Applications: Fundamental Concepts, Biological Interactions and Clinical Applications*. Elsevier; 2019:5-18. doi:10.1016/B978-0-12-816662-8.00002-3

31. Allaker RP, Memarzadeh K. Nanoparticles and the control of oral infections. *Int J Antimicrob Agents*. 2014;43(2):95-104. doi:10.1016/j.ijantimicag.2013.11.002
32. Nguyen Tri P, Nguyen TA, Nguyen TH, Carriere P. Antibacterial Behavior of Hybrid Nanoparticles. In: *Noble Metal-Metal Oxide Hybrid Nanoparticles: Fundamentals and Applications*. Elsevier; 2018:141-155. doi:10.1016/B978-0-12-814134-2.00007-3
33. THOMPSON NR. SILVER. In: *The Chemistry of Copper, Silver and Gold*. Elsevier; 1973:79-128. doi:10.1016/B978-0-08-018860-7.50007-4
34. Kunkalekar RK. Role of Oxides (Fe3O4, MnO2) in the Antibacterial Action of Ag-Metal Oxide Hybrid Nanoparticles. In: *Noble Metal-Metal Oxide Hybrid Nanoparticles: Fundamentals and Applications*. Elsevier; 2018:303-312. doi:10.1016/B978-0-12-814134-2.00010-3
35. Manninen NKA de S. Silver segregation in Ag/a-C nanocomposite coatings for potential application as antibacterial surfaces. Published online 2015.
36. Prabhu S, Poulose EK. Silver nanoparticles: mechanism of antimicrobial action, synthesis, medical applications, and toxicity effects. *Int Nano Lett*. 2012;2(1):32. doi:10.1186/2228-5326-2-32
37. Shan D, Tao B, Fang C, et al. Anodization of titanium in reduced graphene oxide-citric acid electrolyte. *Results Phys*. 2021;24:104060. doi:10.1016/j.rinp.2021.104060
38. Kozhukhova AE, du Preez SP, Shuro I, Bessarabov DG. Development of a low purity aluminum alloy (Al6082) anodization process and its application as a platinum-based catalyst in catalytic hydrogen combustion. *Surf Coatings Technol*. 2020;404:126483. doi:10.1016/j.surfcoat.2020.126483
39. Wang L-N, Jin M, Zheng Y, Guan Y, Lu X, Luo J-L. Nanotubular surface modification of metallic implants via electrochemical anodization technique. *Int J Nanomedicine*. 2014;9:4421-4435. doi:10.2147/IJN.S65866
40. C.A. Grimes GKM. *TiO2 Nanotube Arrays*. Springer; 2009. doi:10.1007/978-1-4419-0068-5
41. Cordeiro JM, Nagay BE, Ribeiro ALR, et al. Functionalization of an experimental Ti-Nb-Zr-Ta alloy with a biomimetic coating produced by plasma electrolytic oxidation. *J Alloys Compd*. 2019;770:1038-1048. doi:10.1016/j.jallcom.2018.08.154

42. Pesode P, Barve S. Surface modification of titanium and titanium alloy by plasma electrolytic oxidation process for biomedical applications: A review. *Mater Today Proc*. Published online December 24, 2020. doi:10.1016/j.matpr.2020.11.294
43. Babaei K, Fattah-alhosseini A, Chaharmahali R. A review on plasma electrolytic oxidation (PEO) of niobium: Mechanism, properties and applications. *Surfaces and Interfaces*. 2020;21:100719. doi:10.1016/j.surfin.2020.100719
44. Wang H, Chu PK. Surface Characterization of Biomaterials. In: *Characterization of Biomaterials*. Elsevier Inc.; 2013:105-174. doi:10.1016/B978-0-12-415800-9.00004-8
45. Ebnesajjad S. Surface and Material Characterization Techniques. In: *Surface Treatment of Materials for Adhesive Bonding*. Elsevier; 2014:39-75. doi:10.1016/b978-0-323-26435-8.00004-6
46. Zhang H. Surface Characterization Techniques for Polyurethane Biomaterials. In: *Advances in Polyurethane Biomaterials*. Elsevier Inc.; 2016:23-73. doi:10.1016/B978-0-08-100614-6.00002-0
47. Salame PH, Pawade VB, Bhanvase BA. Characterization tools and techniques for nanomaterials. In: *Nanomaterials for Green Energy*. Elsevier; 2018:83-111. doi:10.1016/B978-0-12-813731-4.00003-5
48. Duman M, Neundlinger I, Zhu R, et al. Atomic force microscopy. In: *Comprehensive Biophysics*. Vol 2. Elsevier Inc.; 2012:111-143. doi:10.1016/B978-0-12-374920-8.00213-7
49. Wright CJ, Powell LC, Johnson DJ, Hilal N. Microscopy: Atomic Force Microscopy. In: *Encyclopedia of Food Microbiology: Second Edition*. Elsevier Inc.; 2014:666-675. doi:10.1016/B978-0-12-384730-0.00217-2
50. Abhilash V, Rajender N, Suresh K. X-ray diffraction spectroscopy of polymer nanocomposites. In: *Spectroscopy of Polymer Nanocomposites*. Elsevier Inc.; 2016:410-451. doi:10.1016/B978-0-323-40183-8.00014-8
51. Chatterjee AK. X-Ray Diffraction. In: *Handbook of Analytical Techniques in Concrete Science and Technology*. Elsevier; 2001:275-332. doi:10.1016/B978-081551437-4.50011-4
52. Nobre D. Insole Coatings to Prevent Diabetic Foot Infections. Published online 2021.

53. Manninen NK, Calderon S V., Carvalho I, Henriques M, Cavaleiro A, Carvalho S. Antibacterial Ag/a-C nanocomposite coatings: The influence of nano-galvanic a-C and Ag couples on Ag ionization rates. *Appl Surf Sci*. 2016;377:283-291. doi:10.1016/J.APSUSC.2016.03.113

ANNEX A

Firstly, a silicon substrate was ultrasonically cleaned for 10 minutes in Ethanol and 10 minutes in distilled water. Following this step, duct tape was placed on the surface of the silicon sample. Then, mimicking the steps of the silver deposition and using the values represented in Table 0.1, carbon was sputtered onto the surface for 2 hours. The prolonged deposition time was used to create a big step when the tape was removed with the objective of minimizing errors. After the deposition time was over the duct tape was removed, revealing a clean surface without carbon and creating a step between the surfaces with and without carbon. That step was then measured using a perfilometer with the T1 mechanical head, G profile, and an advance of 5.6mm. The perfilometer's results are depicted in Figure 0.1. Using the rule of 3 I was able to calculate the thickness of the carbon layer per minute which rounded the 4nm/minute.

Deposition Time (min)	1	30	60	120
Voltage (V)	623	654	665	665
Current Density (A/m^2)	96.5	91.5	88	81
Power Density (W/m^2)	60000	60000	58750	54000

Table 0.1. Carbon deposition parameters.

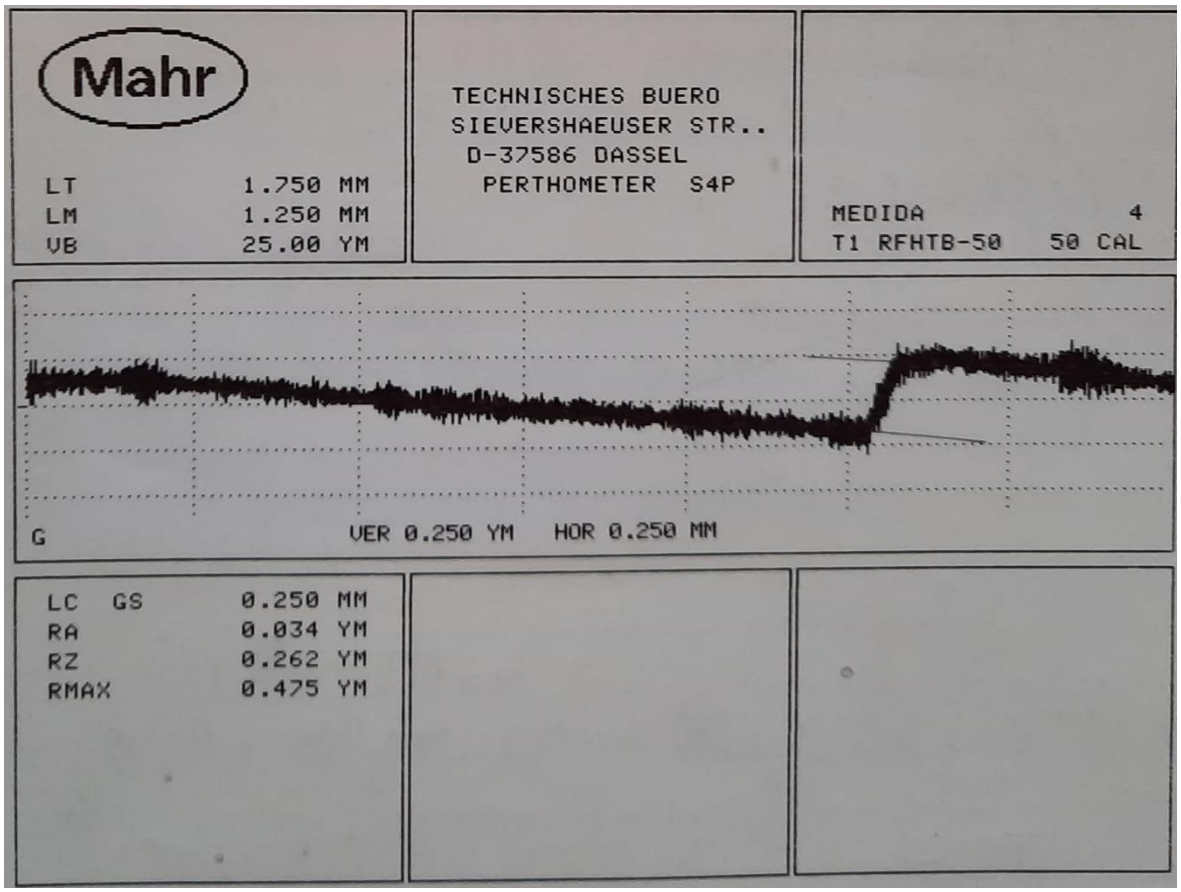

Figure 0.1. Perfilometer results.

[APPENDIX A]

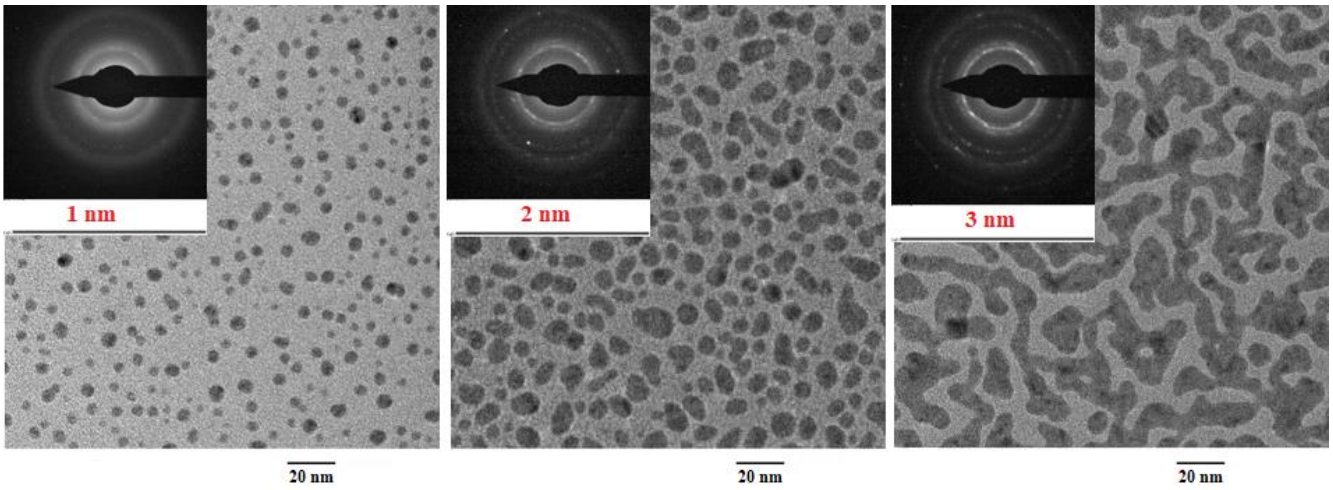

Figure 0.1. TEM grid results.